The Making of a Flight Feather: Bio-architectural Principles and Adaptation

Wei-Ling Chang[1,2,20], **Hao Wu**[1,3,4], **Yu-Kun Chiu**[3], **Shuo Wang**[5], **Ting-Xin Jiang**[5], **Zhong-Lai Luo**[5,6], **Yen-Cheng Lin**[7], **Ang Li**[5,8], **Jui-Ting Hsu**[9,10], **Heng-Li Huang**[9,10], **How-Jen Gu**[3], **Tse-Yu Lin**[3], **Shun-Min Yang**[3], **Tsung-Tse Lee**[3], **Yung-Chi Lai**[1,11], **Mingxing Lei**[1], **Ming-You Shie**[9,12], **Cheng-Te Yao**[13], **Yi-Wen Chen**[4,12], **J.C. Tsai**[3], **Shyh-Jou Shieh**[2,14], **Yeu-Kuang Hwu**[3], **Hsu-Chen Cheng**[7], **Pin-Chi Tang**[7,15], **Shih-Chieh Hung**[1,16], **Chih-Feng Chen**[7,15], **Michael Habib**[17,18], **Randall B. Widelitz**[5], **Ping Wu**[5], **Wen-Tau Juan**[1,3,19,20,*], **Cheng-Ming Chuong**[5,21,*]

[1]Integrative Stem Cell Center (ISSC), China Medical University Hospital (CMUH), Taichung 40447, Taiwan

[2]International Center for Wound Repair and Regeneration (iWRR), National Cheng Kung University (NCKU), Tainan 701, Taiwan

[3]Institute of Physics, Academia Sinica, Taipei 11529, Taiwan

[4]Graduate Institute of Biomedical Sciences, China Medical University (CMU), Taichung 40402, Taiwan

[5]Department of Pathology, University of Southern California (USC), Los Angeles, CA 90033, USA

[6]South China Botanical Garden, Chinese Academy of Sciences, 510650 Guangzhou, China

[7]The Integrative Evolutionary Galliform Genomics (iEGG) and Animal Biotechnology Center (ABC), Department of Life Sciences, National Chung Hsing University (NCHU), Taichung, 40227, Taiwan

[8]Department of Kinesiology, University of Texas at Arlington, Arlington, TX 76019, USA

[9]School of Dentistry, China Medical University, Taichung 40402, Taiwan

[10]Department of Bioinformatics/Medical Engineering, Asia University, Taichung 41354, Taiwan

[11]Research Center for Developmental Biology and Regenerative Medicine, National Taiwan University, Taipei 10167, Taiwan

[12]3D Printing Medical Research Center, China Medical University Hospital, Taichung 40447, Taiwan

[13]Endemic Species Research Institute, Nantou County 552, Taiwan

[14]Department of Surgery, National Cheng Kung University and Hospital, Tainan 701 Taiwan

[15]Department of Animal Science, National Chung Hsing University, Taichung 40227, Taiwan

[16]Drug Development Center, China Medical University, Taichung 40402 Taiwan

[17]Department of Integrative Anatomical Sciences, University of Southern California, Los Angeles, CA 90033, USA

[18]Los Angeles County Museum of Natural History, Los Angeles, CA 90007, USA

[19]Department of Biomedical Imaging/Radiological Science, China Medical University, Taichung 40402, Taiwan

[20]These authors contributed equally

[21]Lead Contact

SUMMARY

The evolution of flight in feathered dinosaurs and early birds over millions of years required flight feathers whose architecture features hierarchical branches. While barb-based feather forms were investigated, feather shafts and vanes are understudied. Here, we take a multi-disciplinary approach to study their molecular control and bio-architectural organizations. In rachidial ridges, epidermal progenitors generate cortex and medullary keratinocytes, guided by *Bmp* and transforming growth factor β (TGF-β) signaling that convert rachides into adaptable bilayer composite beams. In barb ridges, epidermal progenitors generate cylindrical, plate-, or hooklet-shaped barbule cells that form fluffy branches or pennaceous vanes, mediated by asymmetric cell junction and keratin expression. Transcriptome analyses and functional studies show anterior-posterior *Wnt2b* signaling within the dermal papilla controls barbule cell fates with spatiotemporal collinearity. Quantitative bio-physical analyses of feathers from birds with different flight characteristics and feathers in Burmese amber reveal how multi-dimensional functionality can be achieved and may inspire future composite material designs.

Graphical Abstract
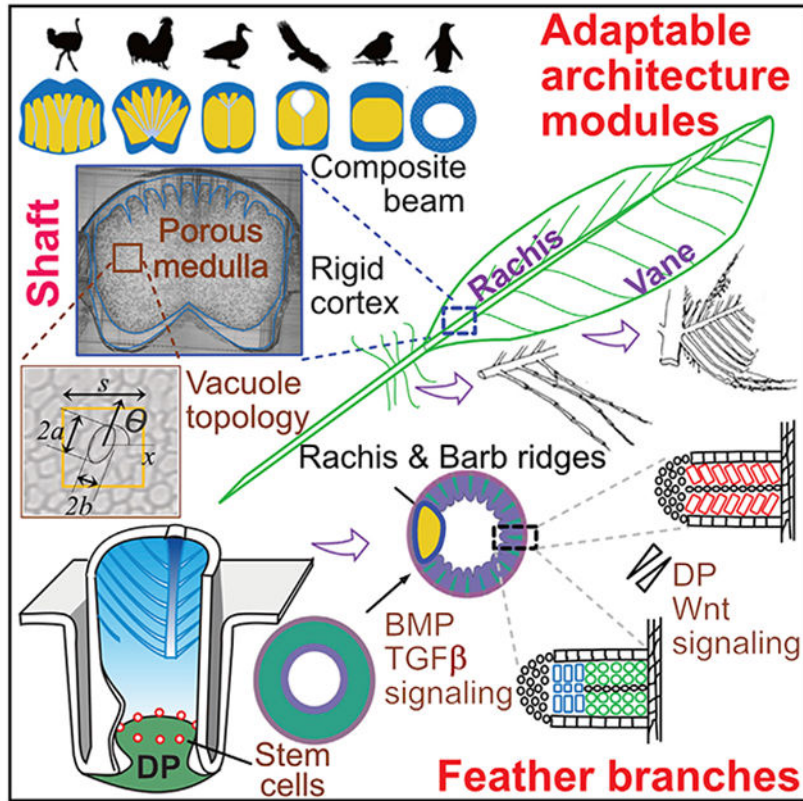
In Brief

The design and developmental paradigms of flight feathers are explored using a combination of bio-physical analyses, molecular characterization, and evolutionary comparisons across a broad range of birds with different flight modes, revealing a modular architectural design that can accommodate diverse ecospaces.

INTRODUCTION

During feather evolution, fluffy plumulaceous branches evolved for thermoregulation and pennaceous vanes for flight and display (Chen et al., 2015; Lin et al., 2013; Prum, 1999; Xu et al., 2014). Fossils of feathered dinosaurs and Mesozoic birds show diverse intermediate feather forms, highlighting the paths taken early in the evolution of avian flight (Benton et al., 2019; Xu et al., 2014). Through at least 150 million years of evolution, the coupling of function and forms optimized feathers for birds to adapt to diverse environments (Bartels, 2003; Chuong et al., 2003; Prum and Brush, 2002).

The pleomorphic functions of feathers are based on the prototypic hierarchical branched architecture composed of rachis, barbs, and barbules (Figures 1A, S1A, and S1B) (Chen et al., 2015; Lucas and Stettenheim, 1972; Maderson et al., 2009; Prum and Brush, 2002). Feathers on a single bird show remarkable macro-region-specific (across the body axis) architectural phenotypes (i.e., flight feathers on the wing, contour feathers on the body, and pennaceous feathers on the tail). Within a feather, micro-region specificity along the

proximal-distal axis enables a single contour feather to have a proximal plumulaceous, fluffy portion to maintain endothermy and a distal pennaceous vane for display and for flight. Yet, during morphogenesis, they are all derived from the interaction of feather stem cells with the dermal papilla (DP) niche (Figure 1B) (Chen et al., 2015; Yue et al., 2005). Tissue transplantation studies show that the DP controls epidermal stem cell fate, implying different branch forms can be modulated based on molecular signals (Yue et al., 2006). To date, most morphogenesis studies have focused on barbs and the formation of feather symmetry (Cheng et al., 2018; Harris et al., 2005; Li et al., 2017; Wang et al., 2011; Yu et al., 2002). Few studies have examined the architectures of the central shaft and feather vane. Both structures are essential for the evolution of flight. Here, we study how a lightweight, strong main shaft (Wang and Meyers, 2016) is made and how fluffy barb branches can be weaved into a planar vane. Together, the remarkable bio-architectures enable diverse flight mode adaptations.

The rachis, a non-uniform tapered beam made of a porous medullary core, and the surrounding dense cortex provide the backbone to support feather weight (Figure 1C, cross-section). The performance of this composite beam depends on its geometry and combinatorial constituents of the medulla and cortex (Bachmann et al., 2012; Gibson, 2005; Laurent et al., 2014; Lingham-Soliar, 2017; Wang and Meyers, 2016). At the molecular level, a Wnt 3a gradient determines the position of the rachis (Yue et al., 2006). A curved rachis in frizzled chickens forms due to a mutated keratin 75 (*K75*) with a defective medulla that alters rachidial rigidity (Ng et al., 2012). Despite this progress, much remains to be learned about how the rachis becomes structured.

The feather vane serves an essential role, yet the molecular basis for transforming the 3-dimensional (3D) barb branches into a 2-dimensional (2D) planar vane is unknown. The barb ridge is the basic structure needed to form feather branches (Chuong et al., 2014; Lucas and Stettenheim, 1972; Prum and Dyck, 2003). Each barb branch is composed of a ramus and two rows of barbules (proximal and distal). As the axial plates disappear from the middle of the barb ridge, the proximal and distal rows of barbules separate and open. In plumulaceous barbs, the distal and proximal barbules have the same shape. In pennaceous barbs, the distal barbules bear a hooklet, a newly evolved subcellular structure, which interlocks onto the proximal barbules of the immediately adjacent barb. This linking occurs via a Velcro-like mechanism to form the closed, coherent surface of the pennaceous feather vane. Basic barb ridge organization allows the flexibility to generate diverse barb branching forms, as seen in different feather types in current birds (Li et al., 2017; Widelitz et al., 2019).

To study how feather architecture can be adaptive in diverse ecospaces, we analyze the rachis and barb branches of feathers. We used a newly developed quantitative morphology field analysis (QMorF) to evaluate the properties of the rachis. Examining different feathers from chickens and flight feathers from birds reveal the importance of medulla cell shape and normalized cortex thickness in endowing feather properties. Molecular studies suggest that transforming growth factor β (TGF-β) signaling is involved in assembling the rachis architecture. We examined cellular and molecular differences leading to the formation of pennaceous and plumulaceous branching. Tissue interactions, transcriptome analyses, and gene perturbation studies show that the DP stores positional information to control feather

branch morphology. We further study feathers embedded in amber ~99 million years ago and found that an ancient feather vane can form by simple overlapping of barbules whereas modern birds use a Velcro-like mechanism.

Our results show that in modern birds, the rachis and barbules evolved distinct architectures for optimal functional performance in their unique eco-spaces. We titled this article the making of a flight feather, in parallel to Lawrence's classical book on animal design (Lawrence, 1992). We aspire to learn similarly fundamental principles that govern feather bio-architectures, enabling birds to adapt to a wide range of eco-spaces. Understanding these principles may also inspire engineers to fabricate light and strong materials for other uses.

RESULTS

Structural Analysis of the Rachidial Cortex and Medulla

To analyze the structure of the rachidial cortex and medulla, we first examined whole mount and serial cross-sections (Figures S1C and S1D) at 1-cm intervals from a 4-week regenerating chicken flight feather that grew to approximately 50% of full length. These specimens demonstrated the gradual maturation of the rachis from young (level I) to older (level IV) developmental stages along the proximal-distal axis. At level I, we see the dorsal cortex start to differentiate but the medulla and ventral cortex have not yet formed. Ridges from the dorsal cortex can be observed at level II. The medulla cells also begin to differentiate at this stage. At level III, both the dorsal cortex and medulla are well differentiated but the ventral cortex remains immature. At level IV, all of the rachis components are mature.

To compare the characteristics of the downy, contour, and flight feather rachis collected when the feathers had reached their full adult size (Figure 1D). Specimens were analyzed at positions along the z axis of the rachis from the beginning of branching at the proximal end (0.0Z) to the distal end (1.0Z) using two methods to assess the internal rachis structure. The first method is synchrotron *micro-computed tomography* (micro-CT) analysis. However, this method caused significant tissue shrinkage (Figures S2A and S2B). As an alternate method, we cut physical cross-sections at different intervals along the proximal-distal axis and then analyzed the properties of the reconstructed rachis. Cortex strength, in general, is a function of its geometry and the material from which it is configured.

Topology of the Medulla—The medulla of the rachis is made of keratinocytes that vacuolized to form one pore per cell. Properties of the medulla are characterized by the size, elongation, and orientation of these pores, collectively. We developed QMorF to provide high-resolution measurements to analyze the spatial distribution of cell shapes and to assess changes in medulla cell structure along the proximal-distal axis (Figure S2C). This method converts multiple cross-sectional images to a digital reconstruction of the medulla with three parameters: pore size (PS) (Figures 1D and S2D), pore elongation (PEL) (Figure S2E), and pore orientation (PO) (Figure S2F).

We analyzed three major types of chicken feathers: flight, down, and contour feathers using QMorF and found that the PS are small and relatively uniform in downy and contour

feathers, but show a large range of variation in flight feathers (Figures 1D and S2D). In flight feathers, PS is small along the midline and at the periphery but is large in the center of each half of the rachis (darker colors indicate larger pore size). This finding suggests these cells are subjected to spatially varied compression/stretching during rachis morphogenesis. The PEL and PO reveal the spatially varied degree of cellular elongation and the direction of the anisotropic stress on the cell, respectively. The PEL was uniformly high in downy feathers, showing a center core in contour feathers, and was highest along cell bands and at the periphery of flight feathers. Cell bands indicate a collective of cells/pores sharing similar geometry that differ from adjacent ones. PEL was close to 1 in the center of the flight feathers (Figure S2E). The range of flight feather PO was much greater than for downy or contour feathers that may reflect the asymmetric feather configuration (Figure S2F). Cell bands are aligned from the dorsal cortex ridge toward the ventral cortex. Beneath the dorsal cortex, medulla cells are orientated perpendicular to the cortical ridge, but cell bands become aligned toward the midline in the ventral medulla. This heterogeneous, yet patterned, organization suggests uneven biomechanical landscapes in the rachis.

Geometry of the Cortex—We further explore the structure-function relationship of rachis architecture in the chicken flight feather cortex. We defined dorsal, ventral, and lateral regions based on their geometric and material characteristics (Figure S3A). We then determined the mean normalized cortex thickness (NCT), to resolve the distribution of dense keratin in these regions. The multiple ridges on the dorsal cortex and the 2 ventral cortex projections on either side of the groove are highlighted as peaks in the angular cortex thickness plot (Figure S3B). Regions showing larger mean NCT suggest a thicker cortex, which would provide greater material strength geometrically. To test the strength of the cortex, a section of rachis (0.3Z–0.4Z) was cut, and the cortex from each of the 4 regions was isolated and subject to a tensile test. The ultimate tensile strength (UTS, the point at which the feather cortex broke) and elastic modulus (E) were calculated (Figures S3C and S3D). Regional cortexes with a larger UTS and E imply their material properties are stronger and stiffer and vice versa.

Structure of the Flight Feather Rachides in Birds Using Different Flight Modes

We wondered whether birds using different modes of flight might have evolved different optimized rachis structures. While flight involves collective feather configurations, wing shapes, and body weight, here, we focus on the biophysical property of the single primary flight feather. We examined the rachis of ostriches (flightless), chickens (short distance flight), ducks and eagles (soaring flight), and sparrows (high wing flapping frequency and bounding flight).

Diverse Medulla Organization in Different Birds—We used QMorF analyses to evaluate medulla cell characteristics in proximal (0.2Z–0.3Z) regions of flight feathers (Figures 2A, S2G, and S2H). For ostriches, the morphological field of the medulla is highly segmented compared to the other species. Heterogeneous vacuolated keratinocytes in the medulla comprise cell bands with a variety of cellular sizes, elongation, and orientation angles. These cell bands show a hyperbolic fanning-out pattern into both the dorsal and ventral medulla, while the ventral cell bands in chickens are merged. As demonstrated by the

ostrich and chicken, the widely spread cell bands, composed mainly of small, elongated, and locally aligned vacuoles, contribute a small average PS, large average PEL, and widely distributed PO. These results suggest that the collectively arranged and aligned cell bands with periodic cortical ridges increases the rachis ability to support mechanical loads.

The bilaterally symmetric QMorF patterns in ducks and eagles are composed of a larger PS, with less significant elongation and angular expansion of vacuoles, suggesting a collective cellular deformation toward the mid-dorsal region. They also both show small cell bands extending from the center toward the ventral groove along the midline. In ducks, the dorsal medulla contains large-sized pores. In contrast, eagles have a hollow cell depletion zone in this same region. These results suggest that enlarged PS improves the stiffness to weight ratio of the rachis by increasing the second area moment of the cortex with limited weight cost and therefore enhances sustained feather flight performance. We also note that the hollow depletion zone in eagles likely increases the tendency of the rachis to twist under load, without greatly compromising bending strength. Although diverse PEL and PO patterns in the medulla provide little benefit to rachis strength, their distribution suggests anisotropic stress applied during rachis morphogenesis contributes to the polarized cortex geometry. The Java sparrow displays a relatively homogeneous medulla. Sparrow PS is like that of the chicken, although their body masses are very different, leading to a much higher pore size/body mass ratio.

We expanded our cross-species QMorF analysis to reveal a trend of functional form at a larger scale. The results show that normalized mean pore size divided by body weight of flight feather shafts, including the rectrix (tail feather) shaft of flying birds (Figure 2B), is, in general, larger than those of other feather types. The mean PS normalized with body weight is a parameter that can represent the function of a feather.

Diverse Cortex Organization in Different Birds—We further analyzed the regional geometric distribution of relative cortex thickness, material strength, and rigidity of flight feathers from the 5 previously described species (Figures 2C and S3E–S3G). These data indicate that cortex polarity seen in flight feathers from the uniform ostrich rachis to the dorsal-ventral polarized eagle rachis. Sustained flyers show a trend of increased thickening in the dorsal cortex and thinning in the lateral cortex (Figure 2C and S3G). The material test also reveals that a polarized flight shaft with a strengthened dorso-ventral cortex and weakened lateral cortex may be a common attribute of flyers that sustain flight for long periods or engage in high flapping frequencies (Figures S3E and S3F). In the ostrich, the cortex was relatively isotropic with a slightly stronger and thicker dorsal wall. These data suggest that sustained flight performance was improved by increasing dorsal-ventral cortex thickness and strength while decreasing these attributes in the lateral cortex. This was accompanied by increasing medulla pore size and decreasing medulla complexity (Figure 2D).

Analyses of Molecular Expression and Function during Rachis Development

To analyze the molecular basis for rachis formation, we performed *in situ* hybridization at different stages of rachis development. H&E staining shows the temporal chicken rachis

morphogenesis from early (Figure 3A, top row) to late (Figure 3A, bottom row) stages of maturity. The rachis is composed of a combination of α- and β-keratins (Figure 3A). We examined the distribution of *K75, Chr25-FK12*, and *K13A* by *in situ* hybridization from early to late stages of maturity. *K75* is expressed by medulla cells (red arrows), *Chr25-FK12* is expressed by cortex cells (green arrows), and *K13A* is expressed by both medulla and cortex cells (blue arrows).

To study how the diverse composite rachides are made, we examined regenerating flight and contour feathers from adult chickens and ducks (Figures 3B–3C′). Immunostaining of K17 (cortex, purple), β-catenin (β-cat, red), and desmoglein 1 (DSG1, green) (cortex and medulla) was examined. In both chickens and ducks, feather epidermal progenitors begin by forming rachidial ridges (Figures 3B and 3C). Thus, the rachis is shaped by the following processes. First, the ventral surface of the dorsal cortex folds to produce different numbers and sizes of cortical ridges. Second, the medulla grows to a certain size. Third, the cortex extends laterally and ventrally to enclose the medulla. Fourth, cells in the medulla become vacuolated and some are organized into cell bands (Figures 3B and S1C). Diverse rachides use these basic processes to different degrees, making a spectrum of composite materials with different phenotypes and physical properties (Figures 1D and S1C).

Feather formation is orchestrated by molecular signaling within the follicle niche (Chen et al., 2015; Yu et al., 2002; Yue et al., 2006). To understand how molecular pathways are used in these morphogenetic processes, we use RCAS retrovirus to mis-express molecules known to be expressed in the developing rachis. Among the ectopically expressed molecules, the most dramatic phenotypes were generated by (1) bone morphogenetic protein 4 (BMP4) that leads to thickening of the dorsal cortex and reduction of the medulla and (2) Ski, a repressor of TGF-β signaling (Tecalco-Cruz et al., 2018), which leads to the inhibition of medulla formation (Figure 3D, enlarged in Figures S4A–S4C). This is reflected by a reduction in the extent of keratin expression after Ski treatment: the elimination of *K75* and *K13A* and disrupted *Chr25-FK12* expression. We measured medulla cell size by examining the cell diameter. Medulla cell size is reduced in both BMP4- and Ski-treated samples. Ski-treated samples show a more dramatic reduction in medulla cell size (Figure S4D, left panel). Control medulla cells are 16–25 μm in diameter. The percentage of cells larger than 16 μm decreased in BMP4-treated samples. Ski-treated samples did not show any cells equal or greater than 16 μm (Figure S4D, right panel). These results imply that the TGF-β pathway may regulate cell differentiation in the cortex and medulla.

Analyses of Molecular Expression during the Development of Barb Branches

To study the formation of the feather vane, we examine how a barb ridge gives rise to pennaceous or plumulaceous barbs (Figure 4A). We use lateral longitudinal sections to examine the barbule structure and cross-sections at the ramogenic zone to discern the barb ridge composition. We explored molecular signaling during different stages of pennaceous and plumulaceous feather formation examining the expression patterns of cell adhesion molecules (α- and β-cat) connexin 43 (Cx43), DSG1, integrin α6 (Int α6), focal adhesion kinase (FAK), liver cell adhesion molecules (LCAM, chicken E cadherin), laminin, and

keratin genes (K5 and K17). We only show β-cat (red), K17 (purple), and DSG1 (green) as examples in Figures 4B and 4C; others are shown in Figures S5A–S5C.

We found that the expression patterns of adhesion molecules differ significantly between pennaceous and plumulaceous branches during development (Figures 4B, 4C, S5A, and S5B). For example, the large barbule cells in pennaceous follicles express β-cat and DSG1 (Figure 4B, panel 16); while in plumulaceous follicles, β-cat is expressed in small cuboid-shaped barbule cells, and DSG1 shows punctate expression in two barbule cell rows (Figure 4C, panel 16). This expression pattern is fundamental and can be used as markers for barb ridges in plumulaceous and pennaceous branches. This expression pattern is also seen in feathers from peacocks and mallard ducks (Figures S6A–S6D).

We further examine barbule cells using high resolution structured illumination microscopy (SIM) (Figures 4D and 4E). In pennaceous branches, longitudinal sections show that β-cat is expressed throughout all hooklets, while DSG1 is enriched in the hooklet periphery. β-cat and DSG1 are partially colocalized (Figure 4D, left panel). Cross-sections show β-cat is expressed throughout the periphery of the hooklet cell, while DSG1 is asymmetrically enriched near the axial plate (Figure 4D, middle and right panels). In plumulaceous branches, longitudinal sections show β-cat and DSG1 are both expressed at the node, but not colocalized between barbule cells (Figure 4E, left panel). Cross-sections show β-cat is patterned as a ubiquitous subcellular net around barbule cells (Figure 4E, middle panel). DSG1 exhibits a polarized distribution, enriched at the side facing the axial plate cells (Figure 4E, right panel).

Dermal Papilla Contains Spatial Information Controlling Branch Patterning

To investigate regional specificity with in the dermal papillacomplex (DP and papilla ectoderm, which is hard to separate), we used a partial DPC ablation strategy (Figures 5A–5C). From the distal to the proximal end, a contour feather is composed of pennaceous branch regions, plumulaceous branch regions, and the calamus (Figure 5D). To test whether different portions of the DP contain information controlling these branch morphologies, we ablate part of the DP. With the anterior DPC removed, the distal pennaceous region diminished (Figure 5E). With the posterior DPC excised, the proximal plumulaceous feather regions disappears (Figure 5F). These results suggest that dermal cells within the DPC contain information that controls feather branch phenotypes.

Transcriptome Analyses Show Asymmetric Expression of WNT Signaling Pathways within the Dermal Papilla

To assess regional DP molecular signaling that regulates the branching phenotype, we performed a non-biased genome-wide expression profile from the anterior and posterior DPC using transcriptome analyses. We identified 886 differentially expressed genes whose cellular functions relate to cell signaling and interactions during multicellular organism processes, organism development processes, as well as cell differentiation. Focusing on signaling pathway members, we found WNT, Hedgehog, and Toll-like receptor signaling pathways, and cytokine-cytokine receptors have unique expression profiles between the anterior and posterior regions of the DP (Figure 5G). The heatmap (Figure 5H) and

scatterplots (Figures 5I and 5J) indicate that WNT ligands and receptors are upregulated in the anterior portion while its inhibitors are upregulated in the posterior region of the DP. This result is further confirmed by quantitative real-time PCR (Figures S6E–S6G). Dynamic differential WNT expression in the DP is also seen during branch formation in other feather tracts (Figures S6H–S6J).

Temporo-spatial Dermal Papilla WNT Signaling Controls Epidermal Progenitor Fate

To evaluate the role of DP WNT signaling in feather branch barbule formation, we perturbed WNT2B levels by injecting small molecular inhibitors or by implanting beads (Jiang et al., 1999) soaked with WNT2B (Figures 5K–5N). We treated the growing pennaceous feather region by placing a WNT inhibitor in the DP; barbule plate cells become disorganized (Figure 5K) and lose their characteristic expression of cell adhesion molecules (Figure 5L). Increased WNT signaling in the anterior portion of growing plumulaceous feather follicles (Figure 5M) exhibits hooklet-like structures and display molecular characteristics of both pennaceous and plumulaceous barbules (Figure 5N). These data suggest that WNT signaling is critical for barbule cell differentiation and is sufficient to induce an identity switch from pennaceous to plumulaceous barbules.

Adaptation of Rachis Architectures Revealed by Feathers of Exotic Birds

To further analyze if the factors effecting rachis structure regulate the mode of flight, we examined the rachis organization in exotic birds that have adapted to live in extreme environments (Figures 6A and 6A′). Emus cannot fly, and feathers from vestigial wings have become fur-like. Both feathers and after feathers form rachis shafts with a concentric cortex and medulla, similar to that of hairs. Ostriches also have lost the ability to fly, and their flight feathers show a different configuration. Ostrich flight feathers have an expanded but non-specialized medulla with thick vacuole walls. There are also regions that have a blurred cortex/medulla identity, implying incomplete cortex-medulla integration. Hummingbirds fly with high-frequency wing flapping, and the wing is almost completely inverted between half strokes (Dakin et al., 2018). Both flight and tail feathers show a shaft with an expanded homogeneous medulla sandwiched by dorsal and ventral cortexes and a very thin lateral cortex (~2 μm), thus producing a feather that is locally symmetric and flexible. The water-diving penguin may need stiffer feathers to maintain feather shape and orientation during movement through water. Indeed, both flight and tail feathers display cortex-dominated configuration. Yet, penguin contour feathers use the opposite strategy, showing a medulla-dominated shaft, with homogeneous vacuoles, probably used for trapping air for thermo-regulation. Thus, the prototypic cortex/medulla composite provides a template that can be modulated for adaptation to diverse environments.

A Different Way to Form a Vane Revealed by Mesozoic Feathers in Burmese Amber

Flight feathers in modern flying birds exhibit distinct distal and proximal barbule shapes, with hooklets that bind to lamella reversibly to form the vane (Figure 6B). Ostriches lost the ability to fly. Their flight feathers show both distal and proximal barbules with similar filamentous shapes that do not interlock to form a vane (Figure 6C). This represents an adaptation, because without flight there is no need to form a vane. We also wonder about the origin of vane formation and whether diverse barbule shapes existed in ancient feathers. We

examine two amber embedded feathers from the Cretaceous period (~98.8 ± 0.6 million years ago) (Shi et al., 2012) that were collected from the Northeast of Myanmar (Figure 6D). Amber embedded feathers preserve extraordinary 3D structures. At each hierarchical level, the filamentous branches (rachis, barb, and barbule) exhibit different morphological features. For orientation, we will use proximal-distal, central-peripheral, and basal-tip to describe the rachis, barb, and barbule, respectively (Figure 6B).

Both CNU A0012 and A0013 are small isolated contour feathers. CNU A0013 is more like a modern pennaceous feather (Figure 6D, top row), while CNU A0012 more closely resembles a modern contour feather (Figure 6D, bottom row). In CNU A0013, the proximal and distal barbules are of similar shapes. The barbule is made of a single row of barbule cells connected head-to-tail. Within a barbule, from the basal to the tip, there are three different cell shapes. Barbule cells close to the ramus are flag-like. There then is a segment of narrow rod-like barbule cells. Toward the tip, the barbule becomes flattened again. No hooklets nor lamella are found in these specimens, yet there is a "primitive" pennaceous-like feather vane produced by overlapping of the flag-like barbules. Adjacent barbs are not tightly connected with each other, and the vanes of these contour feathers may offer limited aerodynamic advantages. CNU A0012 is a contour-like feather (Figure 6D, bottom panels). Along the rachis axis, there are fluffy plumulaceous branches in the proximal and pennaceous-like branches the distal regions. The barbule in the plumulaceous region exhibits a filamentous structure that appears fluffy and curved. Thus, the ancient feathers show the basic architecture of modern feathers but with primitive characteristics.

DISCUSSION

Our multi-disciplinary study reveals how the feather is transformed from a simple one-dimensional filamentous appendage to a three-level branched structure with multi-dimension functionality. At each level, rachis (the main shaft), barb, and barbule phenotypes are under selection pressure for functional optimization at the organism level.

Bio-architectural Principles Used in the Flight Feather

Based on the literature and our own study, we summarize several organization principles that have allowed flight feathers to be flexible, adaptable, and with functional versatility.

1. Being porous. Feathers are made of a central shaft that provides stiffness and lateral vanes that provide aerodynamic lift. In the rachis, the medulla adopted a porous structure comprised of vacuolated keratinocytes. In the vane, the interlocking barbules weave a planar structure that can flap the air.

2. Becoming composite materials. The rachis is a resilient and light composite beam through ingenious integration of the strong solid cortex shell and the medullary core (Wang and Meyers, 2016). The bilayer design makes it easier to adjust the cortex/medulla ratio and the geometrical arrangement freely (van Rees et al., 2017). The result is a spectrum of composite beam structures optimized to afford different mechanical loads required in diverse avian flight modes (Figures 2, 6A, and 6A′).

3. Applying origami principles. Keratinocytes in the medulla are heterogeneous with regions of cell bands composed of vacuolated keratinocytes of distinct sizes, elongation, and orientation angles. Cell bands are arranged collectively under a specific folding field and aligned with periodic cortical ridges to add strength to support mechanical loads.

4. Packaging effectively. Starting from a feather filament cylinder, a series of apoptosis-based "paper-cutting" converts the 2D epithelial sheet into 3D branches. Barbules on neighboring barbs can interlock to provide 2D vanes with a wide range of tunable aerodynamic features or un-hook as needed for cleaning (Sullivan et al., 2016).

5. Achieving functional versatility. Diverse combinations and modulability of each parameter enable many possible designs. Tweaking the topological arrangement of cortex-medulla integration can optimize the composite beam to support the vane with different modes of flight.

The Making of a Flight Feather

The architecture of the feather is based on the formation of hierarchical branch modules: rachis, barbs, and barbules (Chen et al., 2015; Prum and Dyck, 2003). This branched architecture is made by differential sculpting of the filamentous epithelial cylinder (Chang et al., 2004), unlike branching morphogenesis in the mammary gland that is made by differential growth. The mechanisms of barb formation have been explored. Here, we highlight the molecular developmental processes of barbules and rachis, two architectures that have been understudied.

Barbule—The barbule is made of a linear, head-to-tail linkage of barbule cells in a single row. Each barbule cell can exhibit a filamentous, plate, or hooklet shape (Figure 7B). Barbules in plumulaceous regions are filamentous. Barbules in pennaceous regions of current flying birds show lamella and hooklets which use a Velcrolike mechanism to form the vane. We explore the evolutionary origin of this complex Velcro-like apparatus. Architectures of feathers preserved in compressed fossils are flattened but the three-dimensionally preserved feather found in the early-late Cretaceous amber are unique in that they maintain 3D fine structures. Examination of amber specimens show just two barbule cell shapes: filamentous and plate. There is no shape difference between proximal and distal barbules, nor hooklet formation. These ancient barbules form a primitive vane by overlapping proximal and distal barbules of adjacent barbs. This suggests feather vane evolution may have occurred with multiple steps: barbule cell shaping and proper positioning.

We try to identify the molecular control of cell shaping in the barbules, which is a great model to analyze molecular morphogenesis at the single-cell resolution. Asymmetric distribution of adhesion molecules, junction molecules, and cytoskeleton are found in different shaped epithelial barbule cells. We show that hooklet formation is controlled by WNT2B and its antagonists residing in the DP. Remarkably, the distal-proximal topological arrangement of pennaceous/plumulaceous barbules along the rachis is shown to be

controlled by differential anterior-posterior WNT/modulator expression within the DP. The finding provides a mechanism that links the temporal-spatial transcriptomic control of morphogen signaling in the stem cell niche with the regulation of barbule morphogenesis and feather phenotypes in a co-linear fashion.

This result is not just a global disruption of feather formation, because this phenotype is not seen after mis-expressing other signaling pathways. For example, perturbing BMP signaling changed the ratio of the rachis to barbs within a feather, but the pennaceous barb identity was not altered (Yu et al., 2002). Overexpressing gremlin 1 or dominant RAR receptor β changed the ratio of the medial and lateral feather vane, but the pennaceous barb identity was also not altered (Li et al., 2017). Perturbing Wnt3a or DKK1 did alter barb identity. In those experiments, the barbs of flight feathers changed from bilateral to radial symmetry together with the loss of the feather vane (Yue et al., 2006). Hence, modifying WNT signaling through either viral mediated gene transduction of Wnt3a/DKK1 or by applying a WNT2B soaked bead can alter rachis or barb morphology. This is also seen in follicles treating with a FAK inhibitor (Figures S7A and S7B). These results suggest there is a Wnt (in DP)-adhesion molecule-cytoskeleton (in barbule keratinocytes) molecular module that leads to the formation of hooklets, but a detailed mechanism requires further investigation.

Rachis—Rachis formation results from an anterior-posterior Wnt 3a gradient that tilts the radially symmetric barb ridges to generate a rachidial ridge (Yue et al., 2006). The rachidial progenitors are equivalent to differentiating suprabasal cells. These epidermal progenitor cells can generate cortex or medulla, allowing the rachis to adopt flexible composite bilayer structures. Interestingly, the cortex/medulla organizations can differ along the proximal-distal axis (and more so in flight feathers than contour and downy feathers) to provide different mechanical needs in proximal and distal feather shaft. We also explore the evolutionary origin of this organization. Many ancient rachides appear to be rachis-dominated with a narrower barb-forming vane region. The rachis appears to be made of cortex with little to no medulla (O'Connor et al., 2012; Xing et al., 2018). This implies that the early rachis may have used the cortex elongation strategy to provide mechanical strength, and the composite material strategy evolved later as a more adaptive architectural organization.

We try to identify the molecular control of rachis architectures. We found BMP signaling favors cortex formation, while Ski signaling inhibits medulla formation. These results provide a proof of principle of how temporal-spatial control of molecular signaling can be positioned in strategic sites to shape the architecture. From the basis of the BMP/TGF-β pathway, more molecular control of cortex/medulla cell fate specification and how they are arranged topologically to provide the feather shaft with different mechanical strengths will be pursued.

Adaptation and Evolution

The evolution and development of flight involves many changes in the wing and the whole body, yet the flight feather is the basic unit used to build wing shapes. The discovery of fossils of feathered dinosaurs and early birds give clues to the evolutionary path of feather

forms (Lingham-Soliar, 2017; Xu et al., 2014). A primitive vane can be formed by overlapping barbule plates but is less effective in resisting aerodynamic loads. Complexification of barbs and barbules also increase the weight of the feather vane. Eventually, cortex/medulla integration led to the formation of a lighter weight, stronger rachis by optimizing the keratin deposition that could support wider and heavier feather vanes. This enabled the subsequent evolution of stiffer feathers, which allowed high performance of powered flight (Nudds and Dyke, 2010; Wang et al., 2011).

Extant birds provide an opportunity to analyze the flight feathers from birds utilizing different flight modes. In heavier birds, the rachis medulla shows heterogeneous cell bands that are connected with cortical ridges. For chickens, the integrated ridged cortex/medulla may be optimized for short flights or for large body sizes with high load capacity, but this rachis structure may be more susceptible to fatigue-based failure. In songbirds and hummingbirds that featured small body size, high wing flapping frequency, and longer flight durations, rachis simplification with a thin cortex and dominant medulla can become a simple and effective design. The feather architecture can be modulated for various adaptations to produce diverse feather strengths suited to different eco-spaces. (Figures 7A and 7A′).

Overall, we observed two opposing trends: complexification and simplification during the evolution of the rachis and barb branches. In the transition from feathered dinosaurs to flying birds, the earliest flyers may have been relatively large—*Archaeopteryx* was estimated to be only about 200 g, but microraptorines like *Microraptor* and *Changyuraptor* might have massed over 1–4 kg (Dececchi et al., 2016). Initially, rachis complexity has to increase to afford the large mechanical load required for flight (Figure 7A′). In the meantime, barb branches became more complex and produced a more effective vane surface, but at the cost of increased feather weight relative to lift, thus sacrificing efficiency. Feathered dinosaurs ultimately reached a wider range of aerial niches, and we propose that this phase of more sophisticated flight performance was made possible, in part, by innovations of the feather shaft and vane.

The evolution of smaller body sizes (Xu et al., 2014) allow the use of rachis simplification to increase relative structural strength. Thus, in the next phase of rachis evolution, the prior trends may have reversed, with symmetry convergence leading to a simpler and lighter rachis morphology. This trend appears to be in contrast to the morphological symmetry breaking process that generated more diverse and asymmetric feather vanes (Li et al., 2017; Prum and Dyck, 2003). Yet, the vane asymmetry is critical for aeroelastic stability and flight efficiency. Our findings suggest the evolutionary trends of feather shaft and vane are balanced for the best flight performance of an individual bird, and become part of the selective basis of speciation. The principles of functional architectures we studied here may also stimulate bio-inspired designs and fabrication of future composite materials for architectures of different scales including wind turbines, artificial tissues, flying drones, etc.

STAR★METHODS

LEAD CONTACT AND MATERIALS AVAILABILITY

Further information and requests for resources and reagents should be directed to and will be fulfilled by the Lead Contact, Cheng-Ming Chuong (cmchuong@usc.edu). All unique/stable reagents generated in this study are available from the Lead Contact without restriction.

EXPERIMENTAL MODEL AND SUBJECT DETAILS

Animal raising and sample collection—All the animals used in this study were maintained in each institutions animal care facility monitored by trained veterinary staff. Experiments performed follow the approved protocol of the Institutional Animal Care and Use Committees of the University of Southern California (USC), China Medical University (CMU), Taichung, Taiwan, and the National Chung Hsing University (CHU), Taichung, Taiwan. Specific protocol used in different species are listed below.

Chicken—For dermal papilla ablation analyses, rachis development and gene mis-expression experiments, White Leghorn chickens (hatched from SPAFAS eggs provided by Charles River Laboratories, Preston, CT) were used as described below. Approved by USC protocol.

For the barb ridge development and perturbation experiments, three months to one-year old male Taiwan Country chickens were provided by the integrative Evolutionary Galliform Genomics (iEGG), National Chung Hsing University (CHU), Taiwan. Pennaceous and plumulaceous feather follicles were collected at appropriate times as they formed after plucking. Approved by CHU protocol.

For dermal papilla used for RNA-Seq, one-year old male White Leghorn chickens were used. Approved by USC protocol.

Mature shed feathers are collected for QMorF analyses as described below. To investigate the developmental origin of a specific QMorF pattern, we collected regenerated chicken contour feathers and the 1st to 3rd primary flight feathers that grew to 1/2 of the full length (~0.5Z). Approved by CMU protocol.

The following species were used for the QMorF based comparison of PS/body mass—Ju-Chi Native Chicken – Male. Mature shed feathers were collected from a local private farm, Taiwan. Approved by CMU protocol.

Leghorn Chicken – Male. Mature shed feathers were collected from CHU, Taiwan. Approved by CHU protocol.

Red Jungle Fowl – Male. Mature shed feathers were collected from CHU, Taiwan. Approved by CHU protocol.

Silkie Chicken – Male. Mature shed feathers were collected from CHU, Taiwan. Approved by CHU protocol.

Theen-Yee Native Chicken – Male. Mature shed feathers were collected from CHU, Taiwan. Approved by CHU protocol.

Mallard Duck – Male. Mature shed feathers were collected from CHU. Developing follicles were obtained from Mallard ducks kept in iEGG animal facility, CHU, Taiwan. Approved by CHU protocol.

Pekin Duck – Male. Mature shed feathers were collected from the Livestock Research Institute Council of Agriculture, Yilan branch, Taiwan. Approved by CMU protocol.

Barn Swallow – Male. Mature feathers were collected from a taxidermy specimen, from the Wild Bird Society of Taipei, Taiwan. Approved by CMU protocol.

Collared Scops Owl – Male. Mature feathers were collected from 2 bird taxidermy specimens. One was from the Taiwan Endemic Species Research Institute, Taiwan; the other was from the Wild Bird Society of Taipei, Taiwan. Approved by CMU protocol.

Common Moorhen – Male. Mature feathers were collected from a wild animal carcass, from the Wild Bird Society of Taipei, Taiwan. Approved by CMU protocol.

Crested Goshawk – Male. Mature feathers were collected from a taxidermy specimen from the Taiwan Endemic Species Research Institute, Taiwan. Approved by CMU protocol.

Crested Serpent Eagle – Male. Mature feathers were collected from a taxidermy specimen from the Taiwan Endemic Species Research Institute, Taiwan. Approved by CMU protocol.

Domestic Ostrich – Male. Mature shed feathers were collected from Yun Yi Ostrich farms, Taiwan. Approved by CMU protocol.

Emu – Male. Mature shed feathers were collected from 2 birds obtained from Taiwan Boar Town farm. Approved by CMU protocol.

Indian Peacock – Male. Developing feather follicles were collected from one-year old peacocks kept in iEGG animal facility, CHU, Taiwan. Approved by CHU protocol

Japanese White-eye – Male. Mature shed feather, from local pet store, Taiwan. Approved by CMU protocol.

Java Sparrow – Female. Mature shed feather, from local pet store, Taiwan. Approved by CMU protocol.

Night Heron – Male. Mature feather was collected from a taxidermy specimen, from the Wild Bird Society of Taipei, Taiwan. Approved by CMU protocol.

Adelie Penguin – N/A, Mature feather was collected from a taxidermy specimen in the National Museum of Marine Biology and Aquarium, Taiwan. Approved by CMU protocol.

Chinstrap Penguin – N/A, Mature feather was collected from a taxidermy specimen in the National Museum of Marine Biology and Aquarium, Taiwan. Approved by CMU protocol.

Gentoo Penguin – N/A, Mature feathers were collected from 2 taxidermy specimens in the National Museum of Marine Biology and Aquarium, Taiwan. Approved by CMU protocol.

Macaroni Penguin – N/A, Mature feathers were collected from a taxidermy specimen in the National Museum of Marine Biology and Aquarium, Taiwan. Approved by CMU protocol.

Rock Dove – Male. Mature feather was collected from a wild animal carcass, from the Wild Bird Society of Taipei, Taiwan. Approved by CMU protocol.

Ruby-throated Hummingbird – Male. Mature feather was collected from a wild animal carcass, from California. Approved by CMU protocol.

Amber Specimens – Collected from northeastern Myanmar and housed at Capital Normal University (CNU). CNU A0012 and A0013 were analyzed by Shuo Wang who received a Human Frontier Science Program postdoctoral fellowship to travel from China to work at USC.

METHOD DETAILS

X-ray micro-CT—The X-ray micro-CT measurement was performed on the beamline 01A of the Taiwan Light Source (TLS) at the National Synchrotron Radiation Research Center, Hsinchu, Taiwan (NSRRC). The beamline uses a superconducting wavelength-shifter (Song et al., 2007) in the straight section of the TLS storage ring to produce high-flux X-rays (1012 photons/sec) suitable for high speed phase contrast X-ray microtomography (Margaritondo et al., 2004) with a resolution ~1 μm. TLS is operated at 1.5 GeV electron energy and 450 mA.

Polychromatic X-rays (~0.5-2 Å wavelength) were conditioned by a set of slits to limit the beam size at the sample position matching the image field of view. The X-ray photons after penetrating through the specimens are converted by a $CdWO4$ single crystal scintillator to visible light (~560 nm) and captured with an optically coupled cMOS visible light camera (ORCA-Flash 4.0 v2, Hamamatsu, Japan). Attenuators made of single crystal Si wafers can be inserted into the X-ray beam upstream of the specimen to eliminate possible radiation damage to the overall integrity of the specimen and impair the tomography reconstruction process.

However, possible structural modifications by the intense X-rays cannot be completely ruled out, even if the tomography reconstruction is successful (Figure S2A). More subtle changes could occur between tomography imaging due to modification of the materials, for example dehydration. We did observe, for example, shrinkage of the feather rachis between different scans, while not during an individual scan (Figure S2B). We attribute this to be a slower deformation process which occurs after X-ray irradiation and therefore was not picked up in each tomography reconstruction.

A tomography dataset is typically acquired with 600–1000 projection images acquired by rotating the sample with respect to the incoming X-ray beam at fixed rotation steps. Filtered back projection tomography reconstruction is processed by Octopus Imaging software (XRE NV, Belgium), and the reconstructed "slices," then are compiled by the MetaMorph software

(Molecular Devices, USA). The whole process image acquisition, tomography reconstruction and volume rendering takes ~30 minutes for each procedure.

Histology and immunostaining—Feather follicles were collected, fixed in 4% paraformaldehyde at 4°C overnight and 7 μm paraffin sections (both longitudinal and cross sections) were prepared following procedures described (Jiang et al., 1999). Sections were used for hematoxylin and eosin staining, *in situ* hybridization and immunostaining. To remove melanin color, the slides were bleached with H_2O_2 solution as described (Korytowski and Sarna, 1990).

For *in situ* hybridization, sections were dewaxed with Xylene twice (10 minutes each) and then rehydrated with an ethanol series. After washing with PBS twice (5 minutes each), sections were treated with Proteinase K (5 mg/ml, Roche) for 10 minutes. Sections were rinsed with phosphate buffered saline (PBS) twice (5 minutes each) and fixed with 4% paraformaldehyde (Sigma-Aldrich) for 20 minutes. Slides were then washed with PBS twice (5 minutes each), once in 0.1M Triethanolamine (pH 8.0, Sigma-Aldrich) buffer (10 minutes) and then changed to 0.25% v/v acetic anhydride (Alfa Aesar) in 0.1M Triethanolamine buffer (10 minutes). After washing with 2X Saline Sodium Citrate (SSC) solution, slides were dehydrated with an ethanol series and air-dried (30 minutes). 150 μL hybridization solution (50% formamide (Sigma-Aldrich), 5X SSC, 0.1% Tween-20 (Sigma-Aldrich), 0.1% CHAPS (Sigma-Aldrich), 0.5mM EDTA (Sigma-Aldrich), 50mg/ml heparin (Sigma-Aldrich), 0.2 mg/ml tRNA (Roche) and 2% blocking reagent (Roche)) containing probe (0.4 ng/ml) was added to each slide and the slide was covered with a coverslip (Electron Microscopy Sciences). Digoxigenin-labeled probes are from Wu et al. (2015) and Ng et al. (2014). After incubating the slides at 65°C for 16 hours, slides were washed with 2X SSC 3 times followed by 0.2X SSC 3 times (20 minutes each at 65°C). The sections were blocked with 20% goat serum (VWR) for 2 hours and then anti-DIG-AP antibody (1:1000 dilution, Roche) was added and the slides were kept at 4°C for 10 hours. After washing with PBS four times (30 minutes each) and NTMT (0.1M Tris-HCl (Sigma-Aldrich), pH 9.5, 50mM MgCl2 (Sigma-Aldrich), 0.1M NaCl (Sigma-Aldrich)) two times (15 minutes each), NBT / BCIP (Promega) were used to develop the color. Unless otherwise noted, the procedures were performed at room temperature.

For immunostaining, sections were dewaxed and rehydrated as described for *in situ* hybridization above. After washing with PBS twice (5 minutes each), slides were treated with 3% H_2O_2 in methanol (10 minutes) and washed with PBS 4 times (5 minutes each). Sections were blocked with Zeller solution (10mM Tris-HCl (Sigma-Aldrich), 100mM MgCl2 (Sigma-Aldrich), 5% Fetal Bovine Serum (VWR), 1% BSA (Sigma-Aldrich), 0.5% Tween-20 (Sigma-Aldrich), pH 7.4) for 30 minutes. Primary antibodies (1:200 dilution) were applied overnight. After washing in PBS 3 times (5 minutes each), secondary antibodies (1:200 dilution) were applied for 1 hour. The primary antibodies we used were list in Key Resources Table. Secondary antibodies were conjugated to Alexa Fluor 488. Samples stained for β-cat and K17 were pseudocolored red and purple, respectively. Sections were mounted with DAPI histology mounting medium (F6057, Sigma) and imaged with a Zeiss LSM510 confocal microscope or Zeiss ELYRA PS.1 structured illumination microscopy (SR-SIM).

Transcriptome profiling—RNA-seq was performed on samples from dorsal dermal papilla that have regenerated for 3 days after plucking. The anterior and posterior portion of the dermal papilla were dissected and separated. The portions of dermal papilla were further trimmed to leave the anterior or posterior parts. More than 25 follicles from two individual chickens were used to reduce statistical sampling error. The dermal papilla and papilla ectoderm were collected. RNA was extracted using Trizol reagent (Thermo Fisher SCIENTIFIC) with the manufacturer's instructions. For each sample, 2 μg of total RNA was used to construct the RNA-seq library using TruSeq RNA sample preparation v2 kit (Illumina). Two replicates were sent for sequencing performed using Hi-seq 2000 (Illumina) under the 50-cycle single read procedure. For hierarchical clustering, quantification and normalization were performed by Partek Genomic Suit. Further statistical analyses descript below and were done in Partek Genomic Suite, KEGG pathway analysis, and Ingenuity pathways analysis (IPA).

Real-time quantitative PCR—The anterior and posterior portion of dermal papilla were dissected and separated. The portions of dermal papilla were further trimmed to leave the more anterior or posterior parts. More than 25 follicles from two individual chickens were used to reduce statistical sampling error. RNA was isolated with Trizol Reagent (Thermo Fisher SCIENTIFIC) and the concentration was measured with the NanoDrop2000 spectrophotometer. 40 ng of RNA from cells of each treatment condition were used to do reverse transcription with Superscript III (Thermo Fisher SCIENTIFIC). cDNA (150 ng) were used for qPCR using SYBR Green I Master (Roche) with three technical replicates. The sequences of primers specific for genes analyzed were listed in STAR Methods, Key Resources Table. The C_T values were measured by 7500 Real-Time PCR System.

Mis-expression in feather follicle—For suppressing the WNT/β-cat pathway, inhibitor bisdemethoxycurxumin (BDMC) (500 μM, Cayman chemical) or FAK inhibitor PF-573228 (100 μM, Sigma) was microinjected into growing follicles with micropipette. The injection site is near the rachis and close to the dermal papilla. Follicles were collected one week after injection. For ectopic placement of WNT in the anterior of follicle, Affi-Gel® Blue beads (Bio-Rad, 100–200 mesh in diameter) soaked with recombinant WNT2B that including Ser57-Yhr389 (25 μg/250 μL, R&D systems) were implanted into the growing follicle. The site that beads implanted is near the rachis and close to the dermal papilla. Follicles were collected one week after injection.

Transduction of regenerating feather follicles—Pathogen-free, fertilized white leghorn chicken eggs were purchased from Charles River SPAFAS. The eggs were incubated at 38°C in a humidified rotating incubator. Chicks were housed in the University of Southern California vivarium. RCAS–BMP4 and RCAS-Ski plasmids were from P. Francis-West and K. Luo, respectively. Juvenile chickens were anaesthetized with ketamine (50 mg per kg body mass). Primary flight feathers were used to perform RCAS virus injection. Regenerated feather follicles were collected 3 weeks after virus transduction.

QUANTIFICATION AND STATISTICAL ANALYSIS

Parameterization of the rachis with z—We label the proximal-distal axis of the rachis shaft continuously by a parameter z, with zero for the superior umbilical region (SUR), and Z for the distal end. This is done using a set of computer-assisted image analyses (Ng et al., 2012) which involve finding the two lateral edges of the rachis and the midpoint between them. The rachis width is defined as the distance between the two edges of rachis as a function of z.

Serial sections and pre-screening the section for the QMorF analysis—We use the image stack from serial rachis sections for the QMorF measurement. We follow a similar serial section protocol, 5 μm thick sectioning of the parafilm embedding rachis, among the investigated species, except the Ostrich. We used cryostat sections at 5 μm on the ostrich rachides due to their extreme stiffness to ensure the comparability of the QMorF result among our samples.

To minimize technical artifacts due to the serial sections, we perform the following 2-round screening before the QMorF analysis, 1) We eliminate sections that are broken or distorted and are significantly defective; 2) We re-align images of the complete sections using specific morphological landmarks as reference points and then remove sections containing larger local distortions (in general larger than twice the typical coarse graining length scale s). Analysis was performed on more than 8 high quality, 5 μm-thick sections (within a 100 μm z-range) to ensure statistical quality which helped to eliminate artifacts. This analysis also highlighted coherent morphological features embedded in the medulla.

Quantitative morphology field (QMorF)—Under the Olympus BX51 microscope (Olympus Optical, Tokyo, Japan) with a 10X objective, the bright-field images of the 5-mm thick rachis histological sections, embedded either in paraffin (for most rachides) or in a frozen medium (for ostrich rachis only), are captured by a digital SLR camera (Canon EOS 550D, Tokyo, Japan). Prior to extracting parameters that characterize the pores in the medulla section mesh, each image goes through a standardized processing flow, including contrast limited adaptive histogram equalization (CLAHE) enhancement, binarization, cortex and noise removal, and morphological closing, so that every pore can be represented by a single patch.

We then characterize each patch by fitting it to an ellipse describe by semi-major and semi-minor axes (a and b, respectively) and an angle of orientation (Θ). From these three parameters, we study the pore size (PS, defined as πab), the shape (or the elongation PEL, defined as the aspect ratio b/a), and orientation (PO, defined as Θ) statistically (upper panel of Figure S2C).

We define our QMorF as an area-weighted coarse-graining which, more specifically, is to obtain mean values of PS, PEL or PO over an s by s square box centered around each pixel of a cross-sectional image, as a function of (x, y, z) in which images are stacked along the z axis for about 100 μm in total. The typical coarse graining length scale s is six times the mean value of a for the analyzed images in a z-stack (Figure S2C).

Mean PS, PEL, and PO—The extracted morphological quantities of the medulla mesh also provide the statistical distribution of PS, PEL, and PO over a cross-section at a given z (Figure S2G). They are often represented by histograms, from which we calculate not only the mean but also higher moments, to establish our statistical characterizations for the morphology of pores. The statistics are then compared over the height z and over flight feathers of 5 different species (Figure S2H).

Mean normalized cortex thickness (mean NCT)—The contour of the rachis cortex was described by the distances from the geometric center to the inner R_{in} and outer surfaces R_{out} of the cortex (Figures S3A and S3B). We artificially divided the cortex cylinder into four distinct regions, the dorsal (D), ventral (V) and two lateral (L1 & L2) sides as shown in the sketch of Figure S3A. Considering the diverse rachis dimension among species, we calculate the regional mean *normalized cortex thickness* (NCT) defined as

$$\left[2\pi \int_{\theta_i} (R_{out} - R_{in})d\theta \right] \left| \left[\theta_i \int_{2\pi} (R_{out} - R_{in})d\theta \right], \right.$$ where θ_i stands for the angular span of cortex region

i, to compare the four regional cortex thickness in a rachis regardless of its physical sizes.

Characterization of the mechanical properties (elasticity and strength)— Preparation of the rachis: The 2 cm long proximal rachis at 0.4Z was cut first. All barbs were removed, and the rachis was divided into four regions (D, V, L1, and L2 in Figure S3A). Moreover, to obtain the pure cortex of the rachis, the inner medulla of the four regions were removed and prepared to form a dumbbell shape to avoid points of high stress during the tensile test.

Tensile tests: We use a material testing system JSV-H1000 (Japan Instrumentation System, Nara, Japan), with the crosshead speed set at 1 *mm/min* until failure occurs. To calculate the elastic modulus (E) and ultimate tensile strength (UTS), the force-displacement curves of the specimen were converted to stress-strain curves (Figure S3C). The E was obtained using a linear regime of the stress-strain curve, the data points between the 0.005-0.01 strains. The UTS corresponded to the maximum stress on the stress-strain curves (Figure S3D). The E and UTS of the cortex in four cortical regions were obtained by averaging over n > 3 specimens.

Quantification of medulla cell size after RCAS mis-expression—For quantification of medulla cell size afer RCAS-BMP4 and RCAS-Ski mis-expression, we measured medulla cell size by examining cell diameter. Sections in the maturation level similar to Figure 3A, bottom level were used to perform the measurement. The largest diameter of each cell was calculated from 100 cells found in 3 adjacent sections from triplicate biological samples. Cell diameters of treated and untreated samples were compared and statistical significance was determined using the Student's t test.

RNA-Seq data Analysis—Normalized gene expression levels were measured in fragments per kilobase of exon per million fragments mapped (FPKMs) (Mortazavi et al., 2008). Only paired-end reads mapped to the genome without mismatch were used for subsequent analyses. FastQ files were trimmed and mapped to the chicken genome (galGal4)

using Partek Flow. The filtering conditions for our genes of interest were: fold of change > 2 or < −2, maximum RPKM >10, ANOVA with unadjusted p < 0.05. The selected genes were presented by a heatmap with z-scores normalized expression value.

Real-time quantitative PCR analysis—The level of GAPDH is as internal control and each gene expression (CT) was compared with internal control GAPDH (CT = CT - CT mean of GAPDH). Relative quantifications (RQ) were quantified using the delta-delta CT method to compare the values between anterior and posterior of dermal papilla (RQ = 2- CT, CT = CT (anterior) - mean of CT (posterior). Data are expressed as the mean ± standard error of the mean. Two-tailed Student's t test was performed for comparison among groups. P values were considered significant when less than 0.05. Data were plotted using Microsoft Excel.

DATA AND CODE AVAILABILITY

The sequences reported in this paper have been deposited in the GenBank database is NCBI GEO: GSE111008. The data shown in the current study, the MATLAB codes for the QMorF analysis, and materials are available from the corresponding authors upon request.

Supplementary Material

Refer to Web version on PubMed Central for supplementary material.

ACKNOWLEDGMENTS

REFERENCES

Bachmann T, Emmerlich J, Baumgartner W, Schneider JM, and Wagner H (2012). Flexural stiffness of feather shafts: geometry rules over material properties. J. Exp. Biol 215, 405–415. [PubMed: 22246249]

Bartels T (2003). Variations in the morphology, distribution, and arrangement of feathers in domesticated birds. J. Exp. Zoolog. B Mol. Dev. Evol 298, 91–108.

Benton MJ, Dhouailly D, Jiang B, and McNamara M (2019). The early origin of feathers. Trends Ecol. Evol 34, 856–869. [PubMed: 31164250]

Chang CH, Yu M, Wu P, Jiang TX, Yu HS, Widelitz RB, and Chuong CM (2004). Sculpting skin appendages out of epidermal layers via temporally and spatially regulated apoptotic events. J. Invest. Dermatol 122,1348–1355. [PubMed: 15175023]

Chen CF, Foley J, Tang PC, Li A, Jiang TX, Wu P, Widelitz RB, and Chuong CM (2015). Development, regeneration, and evolution of feathers. Annu. Rev. Anim. Biosci 3, 169–195. [PubMed: 25387232]

Cheng D, Yan X, Qiu G, Zhang J, Wang H, Feng T, Tian Y, Xu H, Wang M, He W, et al. (2018). Contraction of basal filopodia controls periodic feather branching via Notch and FGF signaling. Nat. Commun 9, 1345. [PubMed: 29632339]

Chuong CM, Wu P, Zhang FC, Xu X, Yu M, Widelitz RB, Jiang TX, and Hou L (2003). Adaptation to the sky: Defining the feather with integument fossils from mesozoic China and experimental evidence from molecular labo-ratories. J. Exp. Zoolog. B Mol. Dev. Evol 298, 42–56.

Chuong CM, Bhat R, Widelitz RB, and Bissell MJ (2014). SnapShot: Branching Morphogenesis. Cell 158, 1212–1212. [PubMed: 25171418]

Dakin R, Segre PS, Straw AD, and Altshuler DL (2018). Morphology, muscle capacity, skill, and maneuvering ability in hummingbirds. Science 359, 653–657. [PubMed: 29439237]

Dececchi TA, Larsson HCE,and Habib MB (2016). The wings before the bird: an evaluation of flapping-based locomotory hypotheses in bird anteced-ents. PeerJ 4, e2159. [PubMed: 27441115]

Gibson LJ (2005). Biomechanics of cellular solids. J. Biomech 38, 377–399. [PubMed: 15652536]

Harris MP, Williamson S, Fallon JF, Meinhardt H, and Prum RO (2005). Molecular evidence for an activator-inhibitor mechanism in development of embryonic feather branching. Proc. Natl. Acad. Sci. USA 102, 11734–11739. [PubMed: 16087884]

Jiang TX, Jung HS, Widelitz RB, and Chuong CM (1999). Self-organiza-tion of periodic patterns by dissociated feather mesenchymal cells and the regulation of size, number and spacing of primordia. Development 126, 4997–5009. [PubMed: 10529418]

Korytowski W, and Sarna T (1990). Bleaching of melanin pigments. Role of copper ions and hydrogen peroxide in autooxidation and photooxidation of synthetic dopa-melanin. J. Biol. Chem 265, 12410–12416. [PubMed: 2165063]

Laurent CM, Palmer C, Boardman RP, Dyke G, and Cook RB (2014). Nanomechanical properties of bird feather rachises: exploring naturally occurring fibre reinforced laminar composites. J. R. Soc. Interface 11, 20140961. [PubMed: 25339689]

Lawrence PA (1992). The Making of a Fly: The Genetics of Animal Design (Wiley-Blackwell).

Li A, Figueroa S, Jiang TX, Wu P, Widelitz R, Nie Q, and Chuong CM (2017). Diverse feather shape evolution enabled by coupling anisotropic signalling modules with self-organizing branching programme. Nat. Commun 8, ncomms14139.

Lin SJ, Foley J, Jiang TX, Yeh CY, Wu P, Foley A, Yen CM, Huang YC, Cheng HC, Chen CF, et al. (2013). Topology of feather melanocyte progenitor niche allows complex pigment patterns to emerge. Science 340, 1442–1445. [PubMed: 23618762]

Lingham-Soliar T (2017). Microstructural tissue-engineering in the rachisand barbs of bird feathers. Sci. Rep 7, 45162. [PubMed: 28345593]

Lucas P, and Stettenheim A (1972). Avian anatomy. Integument Agriculture Handbook (US Department of Agriculture).

Maderson PFA, Hillenius WJ, Hiller U, and Dove CC (2009). Towards a comprehensive model of feather regeneration. J. Morphol 270, 1166–1208. [PubMed: 19396862]

Margaritondo G, Hwu Y, and Je JH (2004). Synchrotron light in medical and materials science radiology. Rivista del Nuovo Cimento 27 10.1393/ncr/i2005-10004-0.

Mortazavi A, Williams BA, McCue K, Schaeffer L, and Wold B (2008). Mapping and quantifying mammalian transcriptomes by RNA-Seq. Nat. Methods 5, 621–628. [PubMed: 18516045]

Ng CS, Wu P, Foley J, Foley A, McDonald ML, Juan WT, Huang CJ, Lai YT, Lo WS, Chen CF, et al. (2012). The chicken frizzle feather is due to an α-keratin (KRT75) mutation that causes a defective rachis. PLoS Genet. 8, e1002748. [PubMed: 22829773]

Ng CS, Wu P, Fan WL, Yan J, Chen CK, Lai YT, Wu SM, Mao CT, Chen JJ, Lu MYJ, et al. (2014). Genomic organization, transcriptomic analysis, and functional characterization of avian α- and β-keratins in diverse feather forms. Genome Biol. Evol 6, 2258–2273. [PubMed: 25152353]

Nudds RL, and Dyke GJ (2010). Narrow primary feather rachises in Confuciusornis and Archaeopteryx suggest poor flight ability. Science 328,887–889. [PubMed: 20466930]

O'Connor JK, Chiappe LM, Chuong CM, Bottjer DJ, and You H (2012). Homology and Potential Cellular and Molecular Mechanisms for the Development of Unique Feather Morphologies in Early Birds. Geosciences (Basel) 2, 157–177. [PubMed: 24003379]

Prum RO (1999). Development and evolutionary origin of feathers. J. Exp. Zool 285,291–306. [PubMed: 10578107]

Prum RO, and Brush AH (2002). The evolutionary origin and diversification of feathers. Q. Rev. Biol 77, 261–295. [PubMed: 12365352]

Prum RO, and Dyck J (2003). A hierarchical model of plumage: morphology, development, and evolution. J. Exp. Zoolog. B Mol. Dev. Evol 298, 73–90.

Shi G, Grimaldi DA, Harlow GE, Wang J, Wang J, Yang M, Lei W, Li Q, and Li X (2012). Age constraint on Burmese amber based on U-Pb dating of zircons. Cretac. Res 37, 155–163.

Song YF, Chang CH, Liu CY, Chang SH, Jeng US, Lai YH, Liu DG, Chung SC, Tsang KL, Yin GC, et al. (2007). X-ray beamlines for structural studies at the NSRRC superconducting wavelength shifter. J. Synchrotron Radiat 14, 320–325. [PubMed: 17587656]

Sullivan TN, Pissarenko A, Herrera SA, Kisailus D, Lubarda VA, and Meyers MA (2016). A lightweight, biological structure with tailored stiffness: The feather vane. Acta Biomater 41, 27–39. [PubMed: 27184403]

Tecalco-Cruz AC, Ríos-López DG, Vázquez-Victorio G, Rosales-Alvarez RE, and Macías-Silva M (2018). Transcriptional cofactors Ski and SnoN are major regulators of the TGF-β/Smad signaling pathway in health and disease. Signal Transduct. Target. Ther 3, 15. [PubMed: 29892481]

van Rees WM, Vouga E, and Mahadevan L (2017). Growth patterns for shape-shifting elastic bilayers. Proc. Natl. Acad. Sci. USA 114,11597–11602. [PubMed: 29078336]

Wang B, and Meyers MA (2016). Light Like a Feather: A Fibrous Natural Composite with a Shape Changing from Round to Square. Adv. Sci. (Weinh.) 4, 1600360. [PubMed: 28331789]

Wang X, Nudds RL, and Dyke GJ (2011). The primary feather lengths of early birds with respect to avian wing shape evolution. J. Evol. Biol 24, 1226–1231. [PubMed: 21418115]

Widelitz RB, Lin GW, Lai YC, Mayer JA,Tang PC, Cheng HC, Jiang TX, Chen CF, and Chuong CM (2019). Morpho-regulation in diverse chicken feather formation: Integrating branching modules and sex hormone-dependent morpho-regulatory modules. Dev. Growth Differ 61, 124–138. [PubMed: 30569461]

Wu P, Ng CS, Yan J, Lai YC, Chen CK, Lai YT, Wu SM, Chen JJ, Luo W, Widelitz RB, et al. (2015). Topographical mapping of α- and β-keratins on developing chicken skin integuments: Functional interaction and evolutionary perspectives. Proc. Natl. Acad. Sci. USA 112, E6770–E6779. [PubMed: 26598683]

Xing L, Cockx P, McKellar RC, and O'Connor J (2018). Ornamental feathers in Cretaceous Burmese amber: resolving the enigma of rachis-dominated feather structure. J. Palaeogeogr 7, 13.

Xu X, Zhou Z, Dudley R, Mackem S, Chuong CM, Erickson GM, and Varricchio DJ (2014). An integrative approach to understanding bird origins. Science 346, 1253293. [PubMed: 25504729]

Yu M, Wu P, Widelitz RB, and Chuong CM (2002). The morphogenesis of feathers. Nature 420, 308–312. [PubMed: 12442169]

Yue Z, Jiang TX, Widelitz RB, and Chuong CM (2005). Mapping stem cell activities in the feather follicle. Nature 438, 1026–1029. [PubMed: 16355227]

Yue Z, Jiang TX, Widelitz RB, and Chuong CM (2006). Wnt3a gradient converts radial to bilateral feather symmetry via topological arrangement of epithelia. Proc. Natl. Acad. Sci. USA103, 951–955. [PubMed: 16418297]

Highlights

- A cortex/medulla composite beam organization allows rachides to adapt flexibly

- Polarized adhesion and keratin expression lead to hooklet barbules that form vanes

- With-dermal papilla WNT signaling controls barbule shape along the feather P-D axis

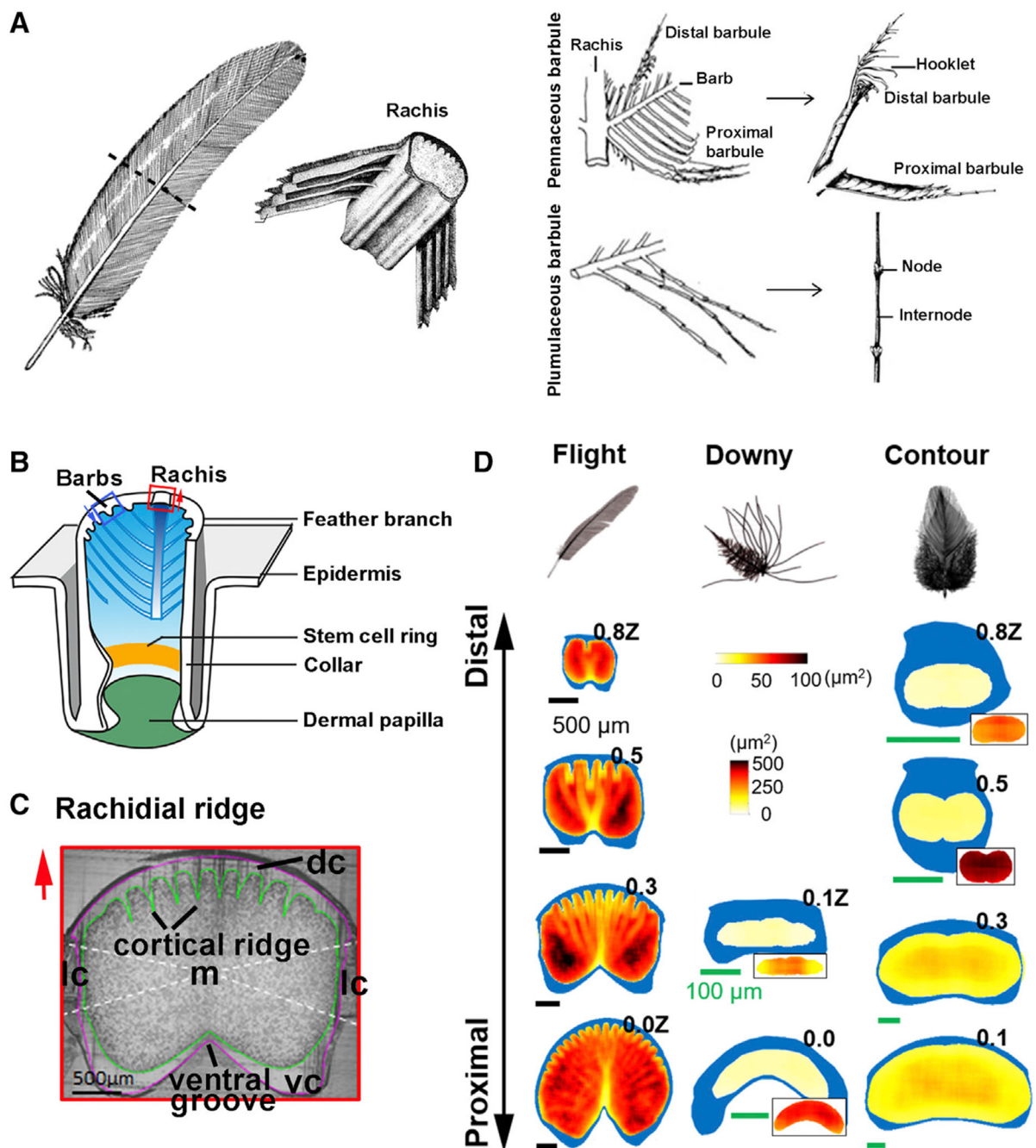- 3D feathers embedded in amber show primitive vanes formed by overlapping barbules

Figure 1. The Cellular Mechanism Guiding the Making of a Feather

(A) Chicken feather schematic, with enlargement of the rachis, pennaceous barbule, and plumulaceous barbule (Lucas and Stettenheim, 1972).

(B) Growth phase feather follicle structure. Stem cell ring in the collar region (yellow stripe). Blue arrows indicate barb ridge orientation.

(C) Chicken flight feather rachis cross-section showing its composition. Cortex is divided into four regions (white dashed lines). Green line surrounds the medulla. Purple line outlines the rachis. Red arrows in (B) and (C) indicate rachis orientation.

(D) Rachis organization along the proximal-distal axis in flight, downy, and contour feathers. The rachis is parameterized along the z-axis (z), where $z = 0$ at SUR (superior umbilical region, junction of the calamus, and rachis) and $z = 1.0Z$ at the distal tip of the rachis. Cortex is depicted in blue. Medulla cell organization is quantified by QMorF measurements. Vertical PS scale is for the main figures, and horizontal PS scale is for the insets. dc, dorsal cortex; lc, lateral cortex; m, medulla; vc, ventral cortex.
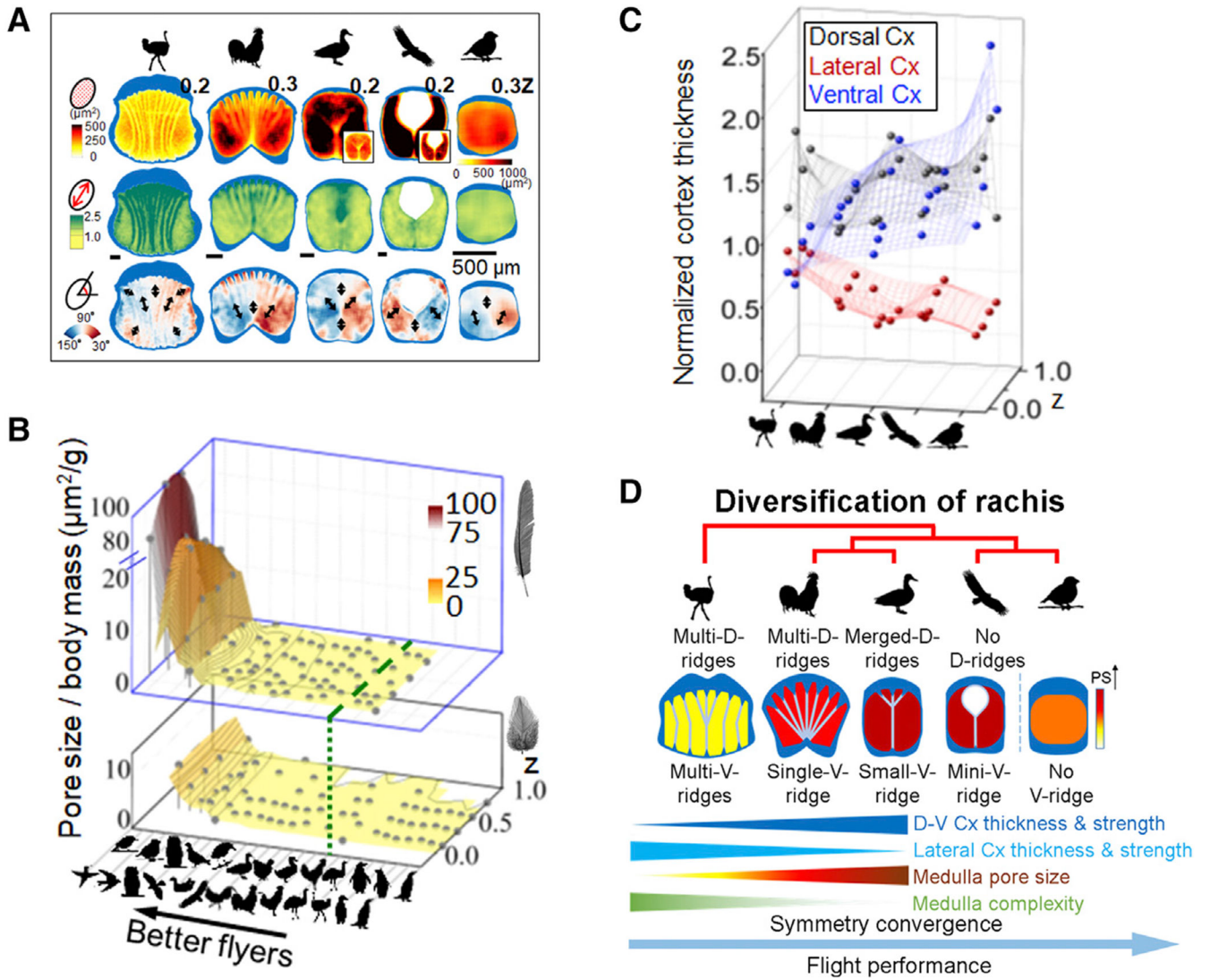
See also Figure S1.

Figure 2. The Internal Architectures of Flight Feather Rachides Are Distinct in Birds Using Different Flight Modes

(A) Flight feather rachides from birds representing five different flight modes analyzed with quantitative morphogenetic field (QMorF) analyses demonstrate the cortex-medulla integration. Three parameters shown from top to bottom rows: distributions of pore size (PS), degree of pore elongation (PEL, i.e., aspect ratio), and pore orientation (PO). Black arrows show polarity of local stresses on vacuoles during morphogenesis. Medulla cell bands stand out as they are composed of medulla vacuole collectives with similar size, shape, and orientation.

(B) Cross species analyses of mean PS normalized by body mass (z axis), in birds with different flight abilities (x axis, high performance flyers, left. Green dashed line marks boundary of flying and flightless birds). Changes along proximal-distal rachidian axes are analyzed (y axis). Pore size/body mass values drop rapidly in flight (top level), but mildly in contour feathers (bottom level).

(C) Cortex changes in birds with different flight abilities. Y coordinate represents mean normalized cortex thickness (NCT) of the rachis. Values along z axis (proximal-distal axis of rachis) are shown.

(D) Trends of symmetrical convergence of rachis topology. Cx, cortex; D, dorsal; V, ventral.
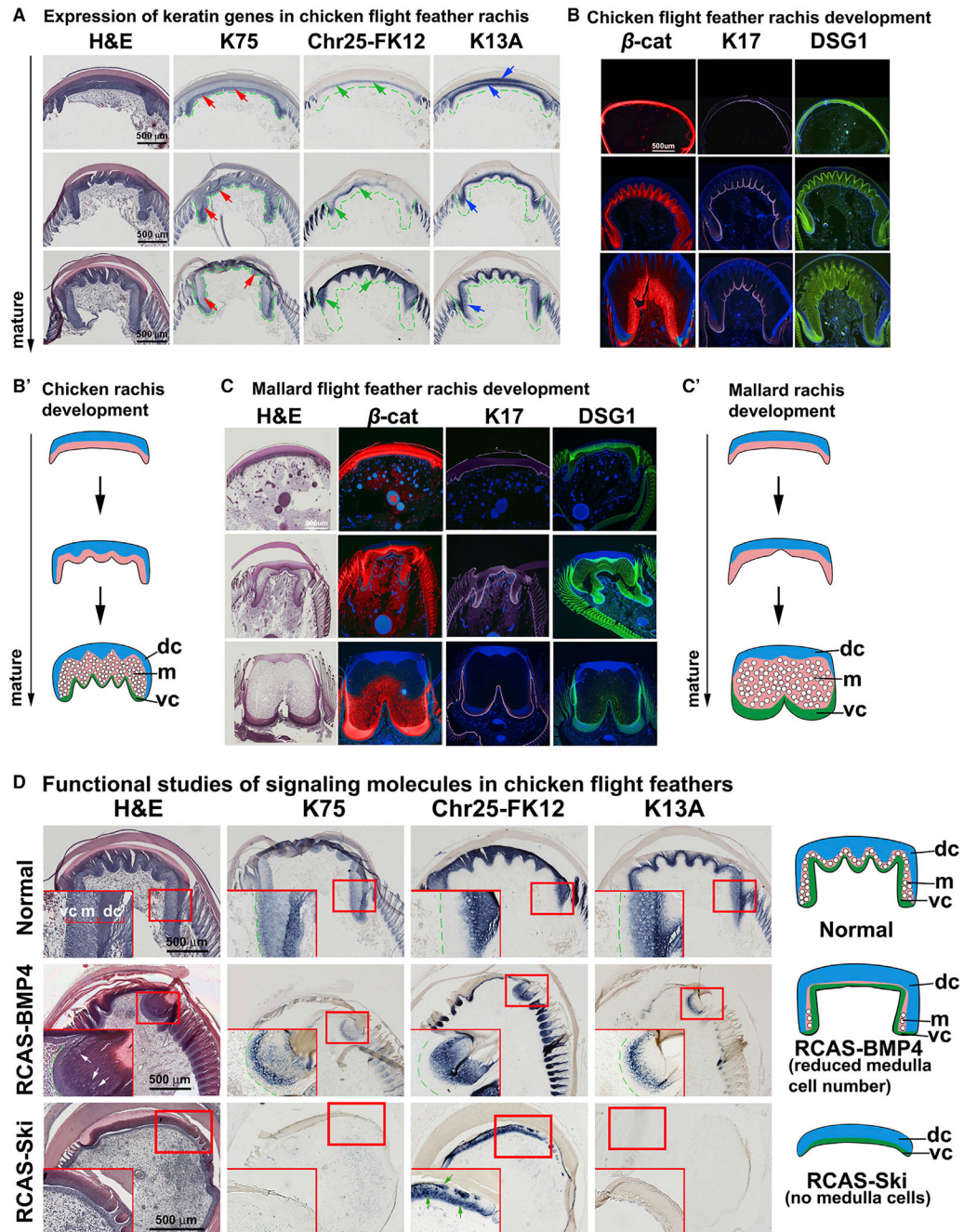
See also Figures S2 and S3.

Figure 3. Molecular Pathways Regulating Cortex and Medulla Organization during Rachis Development

(A) Internal structure and keratin expression in developing chicken flight feather rachides. Increasing maturity, bottom. First column, H&E staining. Second to fourth columns, K75, chr25-FK12, and K13A *in situ* hybridization. Red, green, and blue arrows indicate the expression of K75, chr25-FK12, and K13A, respectively.

(B–C′) Comparison of chicken (B and B′) and mallard duck (C and C′) rachis development. (B and C) Immunostaining of β-cat, K17, and desmoglein 1 (DSG1). Samples are

pseudocolored red (β-cat) and purple (K17) using Photoshop. DSG1 stained images kept the original green color. (B′ and C′) Schematic drawings of different rachis architectures. (D) Functional test of BMP and TGF-β pathways with RCAS-BMP4 and RCAS-Ski perturb rachis morphology. White arrows indicate reduced medulla cells. Green arrows indicate disrupted feather keratin expression. Levels evaluated are similar to (A) (bottom level). chr25-FK12, chromosome 25-feather keratin 12; dc, dorsal cortex; DSG1, desmoglein 1; K13A, keratin 13A; K75, keratin 75; m, medulla; RCAS, replication competent avian sarcoma virus; vc, ventral cortex.
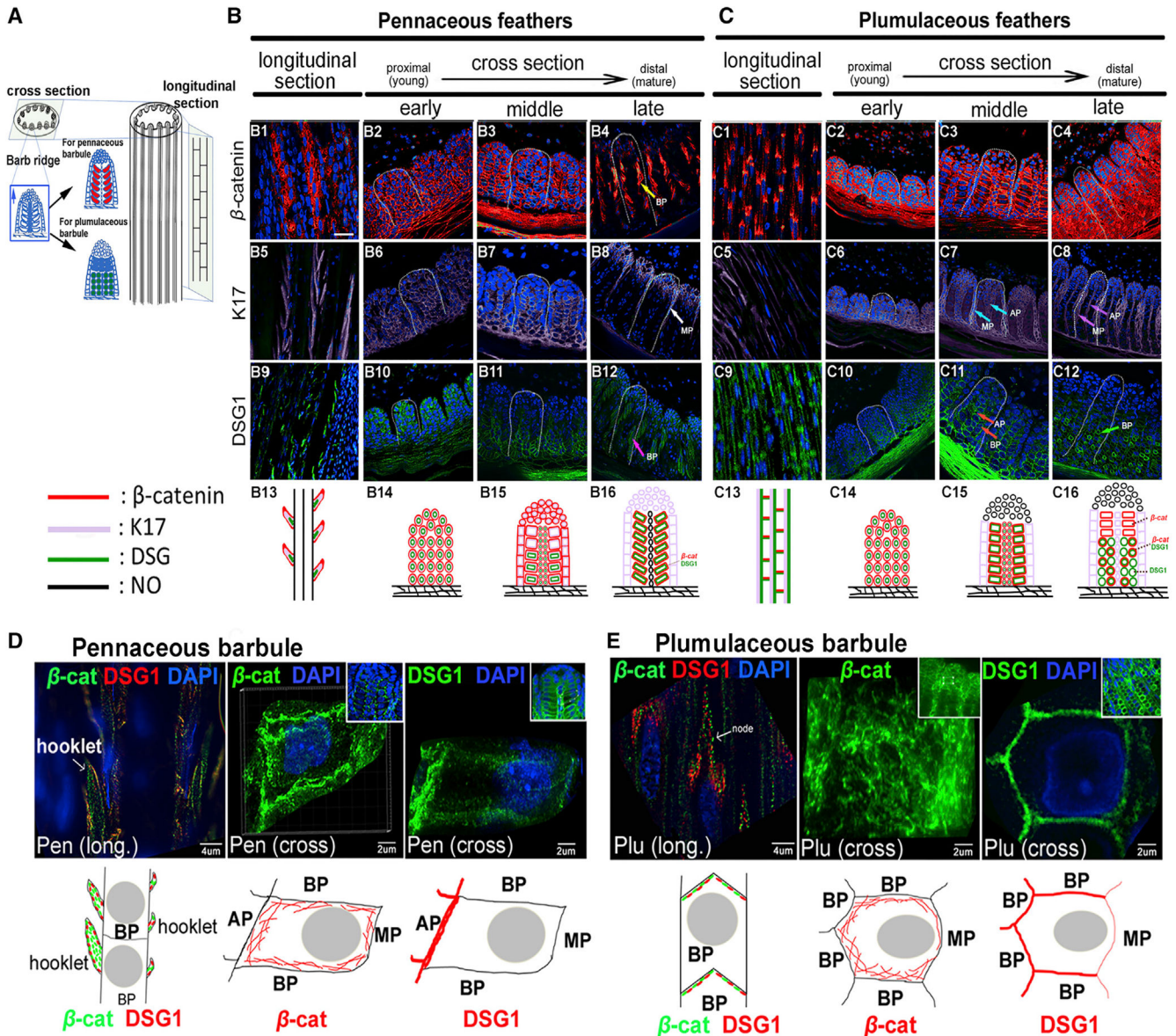
See also Figure S4.

Figure 4. The Morphology of Pennaceous and Plumulaceous Feather Branches Are Marked by Distinct Distributions of Cell Adhesion Molecules and the Cytoskeleton

(A) Feather filament schematic drawing showing epithelial cell arrangements in barb ridge. Undifferentiated barbule primordial cells (blue) can become either pennaceous barbules (red) or plumulaceous barbules (green).

(B and C) Expression patterns of β-cat, K17, and DSG1 are shown in longitudinal and cross-sections in pennaceous (B) or plumulaceous (C) feather branches. White dashed lines outline one barb ridge unit. Bottom panels (B13–B16, and C13–C16) summarize the dynamic molecular expression in each barb region. Stained samples were pseudocolored red (β-cat) and purple (K17) using Photoshop. Images showing DSG1 staining kept the original green color. Expression patterns of these molecules are shown in the schematic diagram using the same colors. No expression is shown in black. Multiple molecule expression is represented with two or three adjacent colors. Scale bar, 15 μm (B).

(D and E) Super resolution microscopy (SIM) imaging of β-cat and DSG1 immunostaining in pennaceous (D) and plumulaceous (E) feather barbules. Insets show lower magnification views. Bottom panels show schematic drawings of each molecule's expression in one barbule cell. Arrows indicate feather branch components. AP, axial plate cell; β-cat, β-catenin; BP, barbule plate cell; Cross, cross section; DAPI, 4′,6-diamidino-2-phenylindole; DSG1, desmoglein 1; K17, keratin 17; Long, longitudinal section; MP, marginal plate cell; Pen, pennaceous barbule; Plu, plumulaceous barbule.
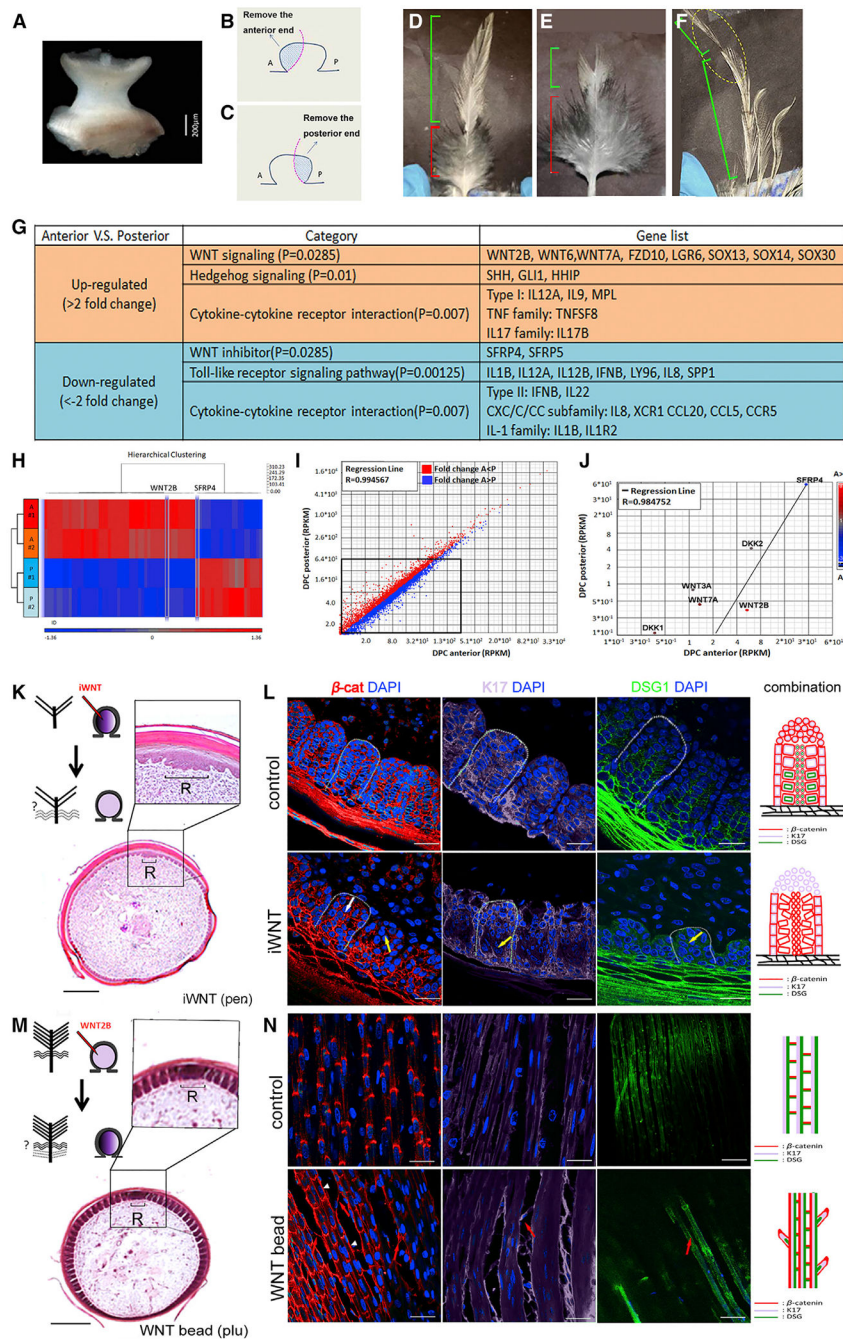
See also Figure S5.

Figure 5. Asymmetric WNT Signaling from the Dermal Papilla Regulates Feather Branch Types by Altering Barbule Cell Shapes

(A–F) Control of barbule morphology by DP niche. (A) Intact DP dissected from growth phase contour feather. (B and C) Schematic drawing shows the strategy used to ablate the DP anterior (B) or posterior (C) regions. Blue region is excised. (D) Normal contour feather with distal pennaceous and proximal plumulaceous barbs. Anterior DP ablation generated feathers that lost the distal pennaceous portion. (F) Posterior DP ablation produced feathers that lost the proximal plumulaceous portion. (D–F) Green bracket, pennaceous branch; red bracket, plumulaceous branch.

(G–J) Transcriptome differences of anterior versus posterior DP. (G) Signaling pathways up- or downregulated in the anterior compared with the posterior DPC region. (H) Heatmap of genes clustered in two groups, anterior versus posterior. (I) Scatterplots depicting transcriptomic comparisons between anterior and posterior DPC regions. (J) Differentially expressed WNT related molecules highlighted in scatterplots.

(K–N) Barbule cell organization alteration by WNT signaling perturbation. (K) Feather branch morphology after applying WNT inhibitor (iWNT) to anterior DP. (L) Barbs in iWNT-treated follicles show disorganized barbule cell arrangement and reduced (yellow arrow) or irregular (white arrow) molecular expression. (M) Feather branch morphology after WNT2B bead insertion to anterior DP. (N) Lateral longitudinal sections display extra hooklet-like structures (red arrow) and irregular β-cat expression pattern (white arrowhead) in plumulaceous region of treated follicles. Colors used in schematic drawings in (L) and (N) match those from Figures 4B and 4C. Scale bar, 200 μm (K and M) and 15 μm (L and N). A, anterior; β-cat; β-catenin; DAPI, 4′,6-diamidino-2-phenylindole; DPC, dermal papilla complex; DSG1, desmoglein 1; iWNT, Wnt inhibitor; K17, keratin 17; pen, pennaceous; plu, plumulaceous; R, rachidial zone; RPKM, reads per kilobase of transcript, per million mapped reads; P, posterior.
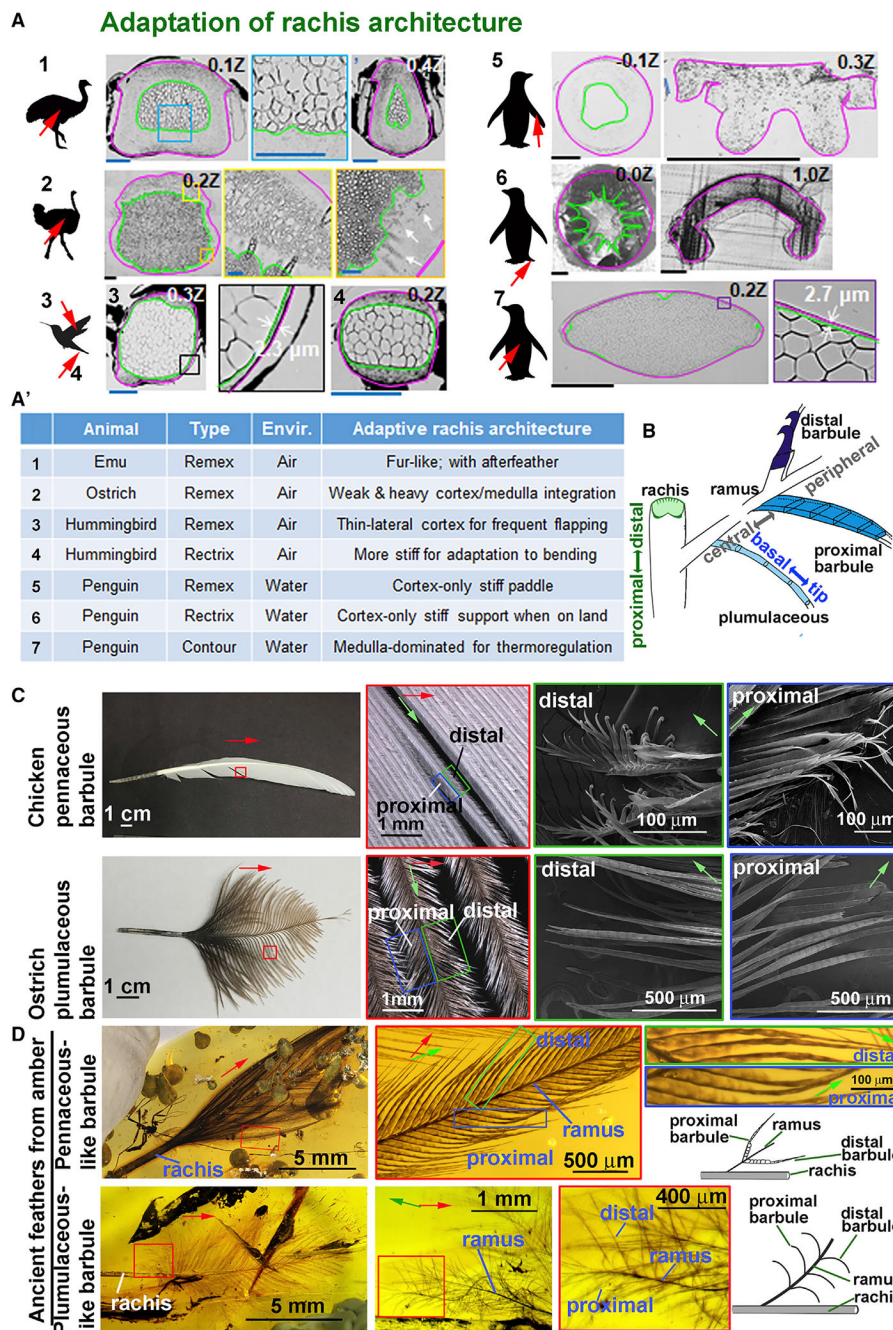
See also Figures S6 and S7.

Figure 6. Diverse Rachis and Barbule Architectures Represent Adaptations of Fundamental Morphological Prototypes
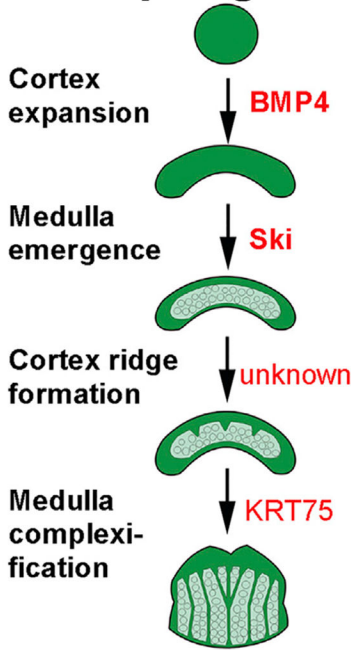
(A and A′) Feather shaft cross sections from birds living in different ecospaces show unique architectural adaptations (A). Feather collection areas, red arrow. Highlight of feather rachis architectural adaptations in different eco-environments (A′). Ostrich body feather rachis dorsal cortex shows a secondary medullary zone (A2, two left panels). White arrows, unclear cortex/medulla identity with vacuoles in the cortex (A2, right panel). Scale bars, blue: 100 μm; black: 500 μm.

(B) Schematic summary of prototypic feather branching architectures depicting rachis with cortex and medulla and barbs with three different barbule shapes: filamentous (plumulaceous), plate, and hooklet (pennaceous).

(C) Detail structure of distal and proximal barbules in adult chicken flight (top row) and ostrich flight feathers (bottom row). Note the loss of hooklets in ostrich flight feathers.

(D) Mesozoic feathers preserved in amber. Top row: pennaceous-like barbs. Bottom row: plumulaceous-like barbs. Pennaceous-like barbules do not display distal and proximal hooklet structures. Green arrows, ramus proximal/distal axis. Red arrows, rachis proximal/distal axis. For (C) and (D), green, blue, and red boxes represent magnified regions of proximal and distal areas.
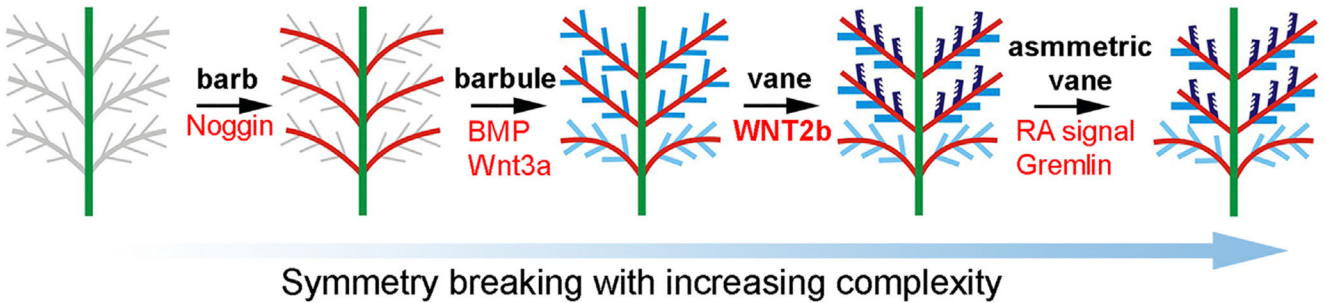
Figure 7. Bio-architectural Principles in Rachis and Barbule Morphogenesis and Their Evolutionary Trends

(A and A′) Representative molecular control and morphological transition during rachis morphogenesis. Conceptual diagram based on data from Figures 1D and 6A (A). Two distinct strategies for optimizing rachis architecture of flight feathers used in birds with burst (i.e., chickens) versus sustained (i.e., eagles) flight modes (A′). Early birds use a powerful shaft architecture and more complex composite beam type architectures. Modern sustained flying birds show a trend toward a simpler design with a strong but light shaft. Based on data from Figure 2.

(B) Schematic drawings showing increased complexity of feather branching morphogenesis. Overall feather shape is based on barb branches that progress from radial symmetry (Harris et al., 2005; Yu et al., 2002) to bilateral symmetric (Yue et al., 2005, 2006), to bilateral asymmetry (Li et al., 2017). Three barbule shapes (Figure 6B), filamentous (light blue),

plate (blue), and hooklet-bearing (dark blue) are shown. Vane formation based on overlapping plate barbules (middle panel) or the hooklet mechanism (2nd from the right) allows fluffy 3D plumulaceous branches to be organized into a 2D vane plane.

KEY RESOURCES TABLE

REAGENT or RESOURCE	SOURCE	IDENTIFIER
Antibodies		
mouse monoclonal anti-β-catenin	BD transduction Laboratories	Cat#610154; RRID: AB_397555
rabbit polyclonal anti-Desmoglein 1 (clone H290)	Santa Cruz Biotechnology	Cat#SC-20114; RRID: AB_2293011
mouse monoclonal anti-α-catenin	BD transduction Laboratories	Cat#610193; RRID: AB_397592
rabbit polyclonal anti-cytokeratin 5	abcam	Cat#ab24647; RRID: AB_448212
rabbit polyclonal anti-cytokeratin 17	abcam	Cat#ab53707; RRID: AB_869865
mouse monoclonal anti-cytokeratin 75	Santa Cruz Biotechnology	Cat# SC-166074; RRID: AB_2134713
rabbit polyclonal anti-Connexin 43	abcam	Cat#ab11370; RRID: AB_297976
mouse monoclonal anti-Integrin α-6	Developmental Studies Hybridoma Bank	Cat#P2C62C4; RRID: AB_528301
rabbit polyclonal anti-Focal adhesion kinase	abcam	Cat#ab4803; RRID: AB_304640
mouse monoclonal anti-L-CAM	Developmental Studies Hybridoma Bank	Cat#7D6; RRID: AB_528115
mouse monoclonal anti-Laminin 5 (clone D4B5)	Millipore	Cat#MAB19562; RRID: AB_94454
goat polyclonal anti-mouse IgG secondary antibody, Alexa Fluor 488	Thermo Fisher Scientific	Cat#R37120; RRID: AB_2556548
goat polyclonal anti-rabbit IgG secondary antibody, Alexa Fluor 488	Thermo Fisher Scientific	Cat#R37116; RRID: AB_2556544
goat polyclonal anti-rabbit IgG secondary antibody, Alexa Fluor 546	Thermo Fisher Scientific	Cat#; A-11035; RRID: AB_2534093
Bacterial and Virus Strains		
RCAS-BMP4	P. Francis-West (Department of Craniofacial Dev. And Stem Cell Biol. King's College, London)	N/A
RCAS-Ski	K. Luo (Department of Mol. Cell Biol., UC Berkeley, Berkeley, Ca)	N/A
Biological Samples		
three months to one-year old male Taiwan Country chicken	integrative Evolutionary Galliform Genomics (iEGG), National Chung Hsing University, Taiwan	N/A
one-year ole male mandarin duck	iEGG, National Chung Hsing University, Taiwan	N/A
Amber embedded feather	This paper	CNU A0012
Amber embedded feather	This paper	CNU A0013
Chemicals, Peptides, and Recombinant Proteins		
Bisdemethoxycurxumin (BDMC)	Cayman chemical	Cat#10960;CAS33171-05-0
Focal adhesion kinase inhibitor	Sigma-Aldrich	Cat#PF-573228; CAS: 869288-64-2
Bovine serum albumin (BSA)	Sigma-Aldrich	Cat#12657; CAS9048-46-8
Affi-Gel® Blue Gel	BIO-RAD	Cat#1537301; CAS: 7732-18-5
Fluoroshield with DAPI	Sigma-Aldrich	Cat#F6057
Trizol	Thermo Fisher Scientific	Cat#15596026

REAGENT or RESOURCE	SOURCE	IDENTIFIER
TruSeq RNA Library Preparation Kit v2	Illumnia	Cat#RS-122-2001
SuperScript III Reverse Transcriptase	Thermo Fisher Scientific	Cat#18080093
LightCycler® 480 SYBR Green I Master	Roche	Cat# 04707516001
Wnt-2b peptide (Ser57-Yhr389)	R&D	Cat#3900-WN/CF; GenPept: O70283
Proteinase K	Roche	Cat#10109495001
Paraformaldehyde	Sigma-Aldrich	Cat#P6148
Triethanolamine	Sigma-Aldrich	Cat#T1502
Acetic anhydride	Alfa Aesar	Cat# 36292-AP
Formamide	Sigma-Aldrich	Cat#F9037
Tween 20	Sigma-Aldrich	Cat#P9416
tRNA	Roche	Cat#10109495001
Blocking reagent	Roche	Cat#11096176001
NBT/BCIP	Promega	Cat#S3771
Fetal Bovine Serum	Gemini	Cat#100-106
Phosphate buffered saline	BioPioneer	Cat#MB1011-10X
SSC Buffer	BioPioneer	Cat#MB1028
Deposited Data		
RNA-seq raw data	This paper	GEO: GSE111008
Oligonucleotides		
Primer: WNT2B Forward: CTCCTCGTGGTGGTACATCG	This paper	N/A
Primer: WNT2B Reverse: ATTGGTACTGGCACTCACGG	This paper	N/A
Primer: WNT3A Forward: TCATCCCGCCTCGGAAGAAA	This paper	N/A
Primer: WNT3A Reverse: AGAGCCTGACTCAACCCACA	This paper	N/A
Primer: WNT4 Forward: CGAGCTGGACAAGTGTGGAT	This paper	N/A
Primer: WNT4 Reverse: CTCCTCGTGGTGGTACATCG	This paper	N/A
Primer: WNT7A Forward: GGTCTCGGGATCCTGTACCA	This paper	N/A
Primer: WNT7A Reverse: TGAGGAAGGTTGGACGCTTG	This paper	N/A
Primer: WNT11 Forward: GACCTGGGTATCGATGGGGA	This paper	N/A
Primer: WNT11 Reverse: GGCTTTCAAGACCTGTCTCC	This paper	N/A
Primer: FZD10 Forward: CTGTGACAGGGACAGTGGTC	This paper	N/A
Primer: FZD10 Reverse: TAACCCACCACAAGGAACTGG	This paper	N/A
Primer: SFRP4 Forward: CCTCTGTTTGCAGATGGGAAG	This paper	N/A
Primer: SFRP4 Reverse: GTTCTTGGCCAGGTAGGTCG	This paper	N/A
Primer: SFRP5 Forward: CCCAGGCTGTGTTCAAGGAA	This paper	N/A
Primer: SFRP5 Reverse: ACAGAGGGTGGGAGTATGGG	This paper	N/A
Primer: DKK1 Forward: GCGACTGATTGCAGTACGTT	This paper	N/A
Primer: DKK1 Reverse: TGGAAACTCAGCGCGTACC	This paper	N/A
Primer: DKK2 Forward: AAGTGGCTAATGGTGCCGC	This paper	N/A
Primer: DKK2 Reverse: TAGCAAGCTTCAGTCCCTGG	This paper	N/A

REAGENT or RESOURCE	SOURCE	IDENTIFIER
Primer: AXIN2 Forward: GCTTACATGAGCAGCAACGG	This paper	N/A
Primer: AXIN2 Reverse: CGTAACCCTCAGCGTTTTGC	This paper	N/A
Primer: LGR6 Forward: TAAAGTCCCTGCTCGCCGAT	This paper	N/A
Primer: LGR6 Reverse: AACCTGCAACCAGGCCAGAC	This paper	N/A
Software and Algorithms		
Partek Genomic Suite	Partek	https://www.partek.com/pgs
KEGG pathway analysis	N/A	http://www.genome.jp/kegg
Ingenuity pathways analysis (IPA)	N/A	https://www.qiagenbioinformatics.com/products/ingenuity-pathway-analysis/
Octopus Imaging	XRE NV, Belgium	N/A
MetaMorph	Molecular Devices, USA	N/A
PhotoShop CS6	Adobe, San Jose, CA, USA	N/A
Computer-aided-design	SolidWorks 2016, MA, USA	N/A
Finite element	ANSYS Workbench, USA	N/A
Adobe Illustrator 4.0	N/A	https://www.adobe.com/downloads.html